222 (2023) 211412

Contents lists available at ScienceDirect

Geoenergy Science and Engineering

journal homepage: www.sciencedirect.com/journal/geoenergy-science-and-engineering

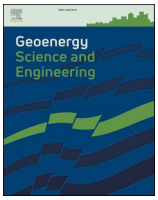

Types and genesis of the Neoproterozoic glauconites, Longshan area, Changping district, Beijing

Qin Zhang [a,b,*], Chen Zhou [c], Shifa Zhu [a,b], Hanyun Tian [a], Ronald J. Steel [d], Zeping Song [a]

[a] College of Geosciences, China University of Petroleum (Beijing), Beijing, 102249, China
[b] State Key Laboratory of Petroleum Resources and Prospecting, China University of Petroleum (Beijing), Beijing, 102249, China
[c] Shengli Oil Production Plant of Shengli Oilfield Company,SINOPEC, Dongying, Shandong, 257000,China
[d] Department of Geological Sciences, University of Texas at Austin, Austin, TX, 78712, USA

ARTICLE INFO

Keywords:
Glauconite
Microstructure
Maturity
Genesis
Qingbaikou system

ABSTRACT

Multiple sets of glauconites occur in the Neoproterozoic outcrops of the Longshan area in Beijing. This study examines the glauconite-bearing clastic rocks of the Qingbaikou System, whose mode of occurrence and genesis remain unclear. The glauconites occur in granular, colloidal, detrital pseudomorphic, pigment-infested and rimmed forms. Considering their varied color, morphology and chemical composition, these glauconites are classified into five types. Type I are granular glauconites with high K_2O and low TFeO content. Type II are yellow-green granular glauconites with low K_2O content. Type III are yellow-brown granular glauconites with strong oxidation. Type IV and V are not considered to be glauconites, in principle. Type IV is a yellow colloidal form whose chemical formula is difficult to determine, while Type V is dark brown detrital glauconite whose chemical composition was altered to form iron oxides. The formation of glauconite is controlled by material sources and redox conditions. Here, the iron components, glauconite and intermediate-basic volcanic rock in the underlying Xiamaling Formation and the felsic conglomerate & coarse feldspar sandstones in the lower Changlongshan Formation are the source for the glauconites in the Changlongshan Formation. The covariant relationship between oxides and maturity levels reveals that Type I granular glauconites have the origin of pseudomorphic replacement of feldspar or quartz. Type II glauconites have a similar trend with the origin of layer lattice theory, and Type III granular glauconites were formed either by early pseudomorphic replacement or layer lattice genesis and later, by alteration. Type IV colloidal glauconites formed under the condition of authigenic cementation in the early stage, most of which were oxidized and altered in the later stage. Type V detrital granular glauconites formed by later re-transportation and allochthonous re-deposition of autochthonous authigenic glauconite or mica pseudomorphic glauconite by the origin of layered lattices. In North China, the presence of Neoproterozoic glauconite makes it difficult to identify the precise systems tract and differentiate the "condensed segments" due to its wide distribution. Different glauconites origins underwent various mechanical and chemical processes, or stages of diagenesis, at various times.

1. Introduction

As a facies indicator mineral, glauconite has applications in determining deposition rates, diagenetic environments, reservoir properties and sequence stratigraphy (Amorosi, 1994,2012; Cecil and Ducea, 2011; Chen, 1980; Chen et al., 2014; Diaz et al., 2003; Ding, 1991; Gopalan, 2008; Gu et al., 2002; Harris and Whiting, 2000; Harder, 1980; Hower, 1961; Huang et al., 1998; Mandal et al., 2020; Smith et al., 1998; Wu, 1992; Yang et al., 2016). Glauconite is a potassium-rich, iron-rich, and water-bearing dioctahedral mica mineral (Baldermann et al., 2013; Banerjee et al., 2015; Su et al., 2016; Zhang et al., 2016). Studies report its occurrence in strata belonging to a wide-span in geological time, from the Precambrian to the Quaternary; glauconite occurs in association with sandstone (Li, 2014; Li et al., 2020), shale (Banerjee et al., 2016a,b; Fürsich et al., 2021), mudstone (Adriaens et al., 2014; Chen, 1994; Wang et al., 2020) and carbonate rocks (Chafetz, 2007; Diaz et al., 2003; Mei et al., 2008; Wang and Wang., 2021; Yang et al., 2020). Depositional environments of glauconite include the continental shelf, slope, and deep sea, as well as tidal flats, lagoons, platforms, deltas, and lakes (Adriaens et al., 2014; Amorosi, 1997; Banerjee et al., 2012; Chafetz,

* Corresponding author. College of Geosciences, China University of Petroleum (Beijing), Beijing, 102249, China.
E-mail address: zhangqin@cup.edu.cn (Q. Zhang).

https://doi.org/10.1016/j.geoen.2022.211412
Received 10 March 2022; Received in revised form 4 December 2022; Accepted 31 December 2022
Available online 4 January 2023

2007; Fürsich et al., 2021; Fernández-Landero and Fernández-Caliani, 2021; Hou et al., 2020; Wu et al., 1997; Wang et al., 2020Wang, 2017).

Glauconites occurs in many forms, including granular, rimmed, colloidal, biofilm-like, and pigment-infested forms (Baioumy and Boulis, 2012a; Burst, 1958; Zhang, 2018; Zhang et al., 2016), all of which have different genesis mechanisms (Bansal et al., 2018; Chang, 1992; Chen, 1987; Fischer, 1990; Li, 2014; Tounekti et al., 2021). The origin of granular glauconites is attributed to grain verdissement (Odin and Matter, 1981) or layered lattice theories (Burst, 1958; Hower, 1961). Colloidal or cemented, rimmed glauconites are a result of pesudomorphic replacement (Banerjee et al., 2008, 2016) or authigenic cementation (Kazerouni et al., 2013; Mei et al., 2008; Zhang et al., 2016). The occurrence and distribution of glauconites is complex (Baioumy and Boulis, 2012a; Hegab et al., 2016; Fernández-Landero and Fernández--Caliani, 2021; Li, 2014; Zhang et al., 2017a), and the various genesis hypotheses proposed have limitations in explaining the formation and evolution of glauconites under varying evolutionary conditions.

Glauconites occur in the Neoproterozoic Xiamaling, Changlongshan and Jingeryu Formations. Previous studies have discussed the characteristics and formation environment of the glauconites developed in the Mesoproterozoic Tieling Formation in the Jixian area (Mei et al., 2008; Mei, 2018; Zhou et al., 2009), the Paleoproterozoic Xiong'er Group (Xu et al., 2010) and the Neoproterozoic rocks in the Liujiang Basin (Chu et al., 2022) in North China. The occurrence and genesis of glauconites developed in the Neoproterozoic strata in the Longshan area of Beijing have not been studied. This study discusses the occurrence, chemical composition, and maturity of glauconite from the Neoproterozoic glauconite-bearing clastic rocks in the Longshan area. The differences in the genesis and evolution patterns of varied glauconites are studied based on their chemical composition and their covariant relationships, sources, maturity, and formation conditions.

2. Materials and methods

2.1. Geological background

The study area is in the Longshan area of the Changping District, Beijing (Fig. 1a) and in the Precambrian, was part of the northwest Yanliao Rift Trough (Fig. 1a) (Bai and Dai, 1994; Fan, 2015; Guo et al., 2019). The Yanshan Rift Trough formed as a result of the large-scale breakup of the crystalline basement in the Changchengian period (Pan et al., 2013; Tang et al., 2016). This area has experienced four major tectonic events between the Archean and the present (Qu et al., 2012). The sedimentary evolution of the thick tensional rift-faulted depression in the Changchengian period resulted in the balanced load deposits of the Jixianian period, which formed the caprock deposits of the Qingbaikou System (Fig. 1b). The Changcheng, Jixian and Qingbaikou systems are mixed rocks of clastic and carbonate components (Zhou et al., 2006). The Qingbaikou System is divided into the Xiamaling, Changlongshan and Jingeryu Formations (Wang et al., 2000; Zhang et al., 2020; Zhu et al., 2012). Recent dating results classify the Xiamaling Formation into a new system (Zhu et al., 2012). The glauconites exist in sandstone, siltstone and shale of the Xiamaling and Changlongshan Formations, and in the calcareous sandstone at the bottom of the Jingeryu Formation. Carbonate and mudstone rocks make up much of the Cambrian strata, while the Jurassic is dominated by pyroclastic and volcanic rocks (Yang et al., 2020; Zhang et al., 2020).

Samples for this study were collected from the Changlongshan and Xiamaling Formations. In the Xiamaling Formation, gray-green and gray shales are interspersed with lenticular fine sandstones and siltstones. They were likely formed in shallow continental shelf, subtidal shoal belt, sand flat, and subaqueous lagoon environments. The Changlongshan Formation can be sub-divided into three parts; the lower part is made up of conglomerates and gravel-bearing feldspar-rich coarse sandstones, the middle has quartz sandstones and glauconite sandstones, and the upper part has interbedded purple-red and gray-green shales. The

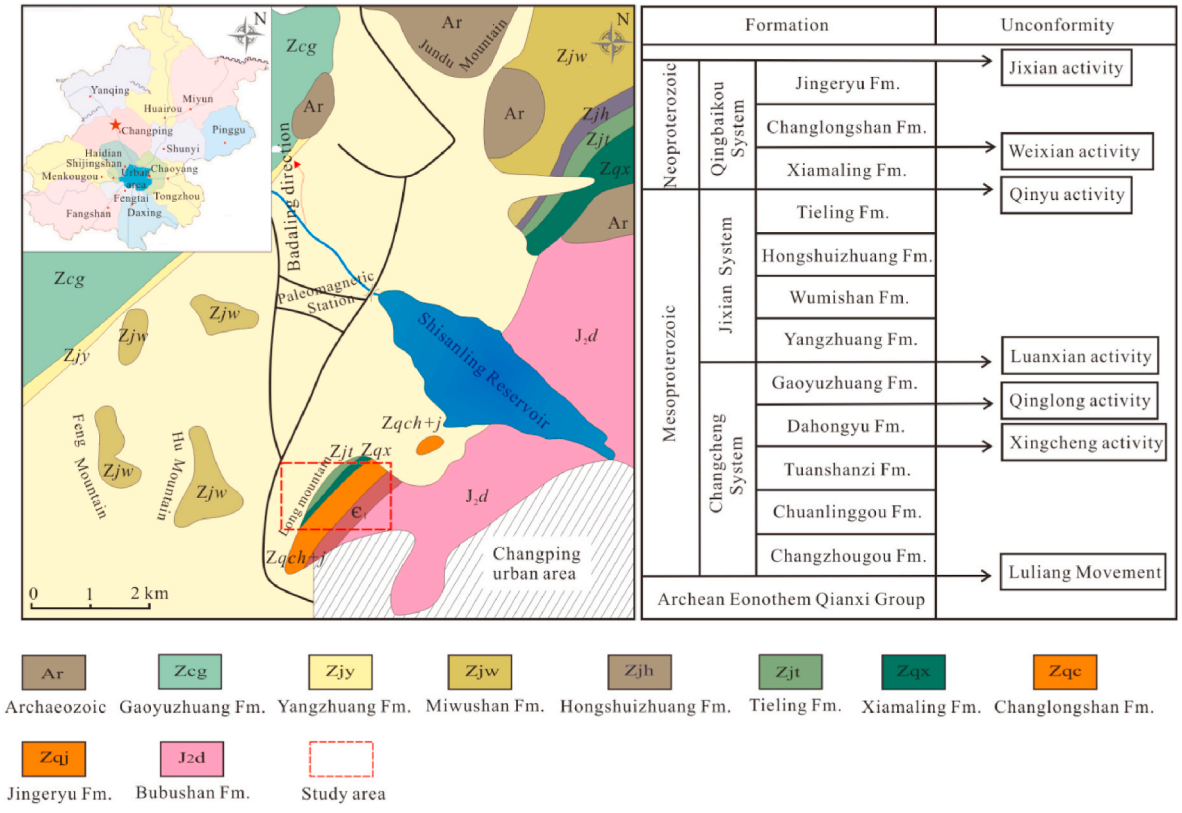

Fig. 1. Location of the study area and the developmental characteristics of the Mesoproterozoic and Neoproterozoic in North China.

depositional environment for the Changlongshan Formation is likely related to tidal flat settings such as tidal channels, sand flats, subaqueous shoals, and underwater lagoons (Fig. 2).

2.2. Methods

A total of 79 samples were collected for this study; these include glauconites and iron sandstones from the Changlongshan Formation and glauconite siltstones and shales from the Xiamaling Formation (Fig. 2). In addition, the experimental analysis includes petrography (38 groups), grain surface texture (12 groups), geochemical element analysis (12 groups), mineral composition analysis (10 groups), and (REE + Y) studies (7 groups).

A Nikon Eclipse LV100N POL polarizing microscope was used to observe the morphology of the glauconite, and a SU8010 high-resolution field emission scanning electron microscope was used to characterize the microstructure and surface morphology. For these analyses, the accelerating voltage field was 30 kV, the working distance was 15 mm, and morphological characterization was performed using electron probe (SE) imaging technology. In addition, compositional differences were analyzed by a backscatter probe (SSD). Autochthonous quantitative analysis of microscopic components was done using a EDAX GENESIS2000 X-ray energy dispersive spectrometer (EDS). In order to enhance the electrical conductivity of the samples, an Au layer with a thickness of about 10 nm was sprayed on the flat sample surface using an ion sputterer. Electron probe testing was performed using a JEOL JXA-8100 electron probe microanalyzer. The REE + Y analysis was first performed by micro-drilling the polished surface of the rock, and then tested using a PE300Q ICP-MS instrument with an accuracy greater than 10%. Trace element analysis was performed using an inductively coupled plasma mass spectrometer (instrument model ICAP-RQ). After being vaporized, the samples entered the central region of the ion body in the form of aerosols and were converted into positive ions. Furthermore, the contents of various elements in the samples were determined based on the peak intensities of their mass spectra. The ICP emission power was 1550 W, the auxiliary gas flow was 0.8 L/min, the atomizer flow was 1.1 L/min, and the standard liquid concentrations were 0, 40, 100, 160, and 200 μg/L, respectively. Moreover, the MS pump speed was less than 40 RPM, and the CCTI flow rate was 5.525 L/min.

In this study, the anion method based on $O_{10}(OH)_2$ was used to calculate the ionic structures of different types of glauconite, after which their different chemical formulae were derived. The test results of trace elements reflect the geochemical properties of the source rocks. In this study, we use the La–Th-Sc, Th–Co–Zr/10, Th-Sc-Zr/10 discriminative charts to analyze the tectonic setting (such as oceanic island arcs, continental island arcs, active and passive continental margins), and use the covariant relationships of La/Th–Hf and La/Sc–Co/Th to analyze glauconite substrate rock types (Condie, 1991; Gu et al., 2002; Zhang et al., 2020) to evaluate the material source, and determine the formation and evolution process of glauconite.

3. Results

3.1. Classification of glauconite forms

Petrological observations suggest that the glauconites in the Longshgan area have granular, pseudo-like, colloidal, rimmed, and pigment-infested forms (Fig. 3). Granular glauconites are divided into autochthonous granular glauconite (Fig. 3a, b, c, d, e) and allochthonous detrital granular glauconite (Fig. 3f). Autochthonous granular glauconites vary in color from green (Fig. 3a and b) and yellow-green (Fig. 3c and d) to yellow-brown varieties (Fig. 3e). Allochthonous detrital glauconites are dark brown, and their rounded grains reflect the transport and abrasion of tractive flows in the later stages (Fig. 3f).

Glauconites in the Xiamaling Formation are formed by mica alteration. They retain the shape of the original mica, and named as clastic pseudomorphic glauconites (Fig. 3g). This kind of granular glauconite may be formed by the halmyrolysis of mica, making it autochthonous.

Colloidal glauconites are formed between quartz grains (Fig. 3h and i). Their color is a light yellowish-brown, and they form thin films between the quartz particles and their overgrowth edges (Fig. 3j). This indicates that the glauconites were formed after the quartz overgrowth.

Under the microscope, the yellow-brown glauconites appear to grow around the light yellow-green granular glauconites in the form of rimmed edges (Fig. 3k). This suggest that the rimmed edges and the glauconite core particles were formed at different stages. The glauconite core is an early-formed granular glauconite, while the rimmed edge belongs to the later-stage cement.

The pigment-infected glauconites (Fig. 3l) are sporadically distributed at the edges, interiors, or microfractures of quartz or feldspar grains. They are yellowish-brown, and are formed by local metasomatism of substrate particles. They are the products of the early granular glauconites (Wu et al., 1997; Zhang et al., 2016).

Granular, colloidal, pigment-infested, and rimmed halo-rimmed glauconites are autochthonous. There is also a difference in the composition and genesis of glauconites with different colors and forms. The glauconites are further divided into five types: Type I are light green granular glauconites (Fig. 3a and b); Type II are yellow-green granular glauconites, (Fig. 3c and d); Type III are yellow-brown granular glauconites (Fig. 3e, g), including pseudo mica-like glauconites; Type IV are yellow-brown colloidal (Fig. 3h) and rimmed glauconites (Fig. 3k); Type V are detrital allochthonous granular glauconites (Fig. 3f). The first four types (I ~ IV) belong to the autochthonous glauconite, and the Type V belongs to the autochthonous glauconite. "Pigment-infested glauconites" are autochthonous glauconites formed in the diagenetic period (Baioumy and Boulis, 2012a; Zhang et al., 2022). They mainly exist in the micro-pores or cracks of the substra particles, and represent the early stage of metasomatic granular glauconites (Type II).

3.2. Glauconite microstructures

Glauconites of different maturity have varied microstructures (Amorosi et al., 2007; Banerjeeet al., 2016; Zhang et al., 2016). Those that form initially are small amorphous particles; they adhere to each other, forming 2–3 μm-sized caterpillar-like aggregates. Lamellar structures that gradually develop on the surfaces of these glauconites, represent a mature stage. Eventually, the glauconites that have entered the high maturity stage into flower-like clusters. The surface morphology of allochthonous glauconite particles is partially or completely destroyed during their transport, which makes the particle surface flat.

Glauconite microstructures in this study vary under the SEM. Glauconites have complete grain shapes at low magnification and sheet-like structures (Fig. 4a); the colloidal glauconite fills the tiny gaps at the edge of quartz grains (Fig. 4b); the cement-like glauconite fills in a large area between the quartz grains (Fig. 4c); the immature rims wrap around the highly mature grain cores, forming a halo-like structure (Fig. 4d). Observations show that most of these glauconites have a parallel lamellar, curved lamellar or splintery microstructure in the Xiamaling and Changlongshan Formations (Fig. 4e,f,g). Hairball-shaped glauconites are relatively immature and belong to the early-stage glauconites. With increasing maturity, glauconites, exhibit a nearly parallel lamellar microstructure (Fig. 4e). These glauconites formed in an environment with sufficient growth space and exhibit relatively higher maturity. When the growth space is more compact, the number of parallel lamellar structures of the glauconites reduce considerably, glauconites can exist in the form of curved lamellar (Fig. 4f) or splintery microstructure (Fig. 4g). Microscopic observations suggest a symbiotic relationship between glauconites and minerals such as quartz, iron oxide, siderite, pyrite, ankerite and collophanite (Fig. 4b,c,e, h).

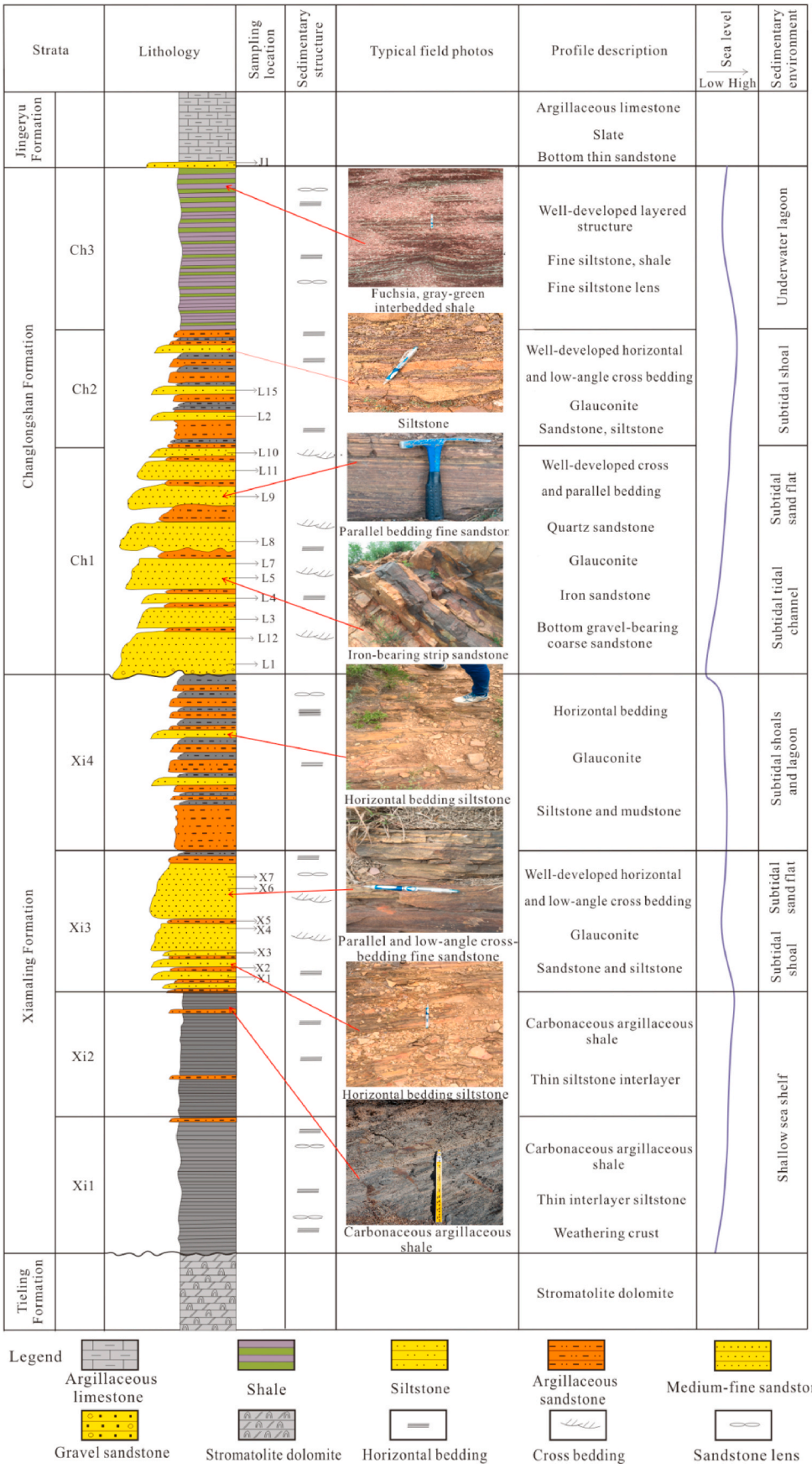

Fig. 2. Comprehensive sedimentary histogram of the Qingbaikou System in the Longshan area, Beijing.

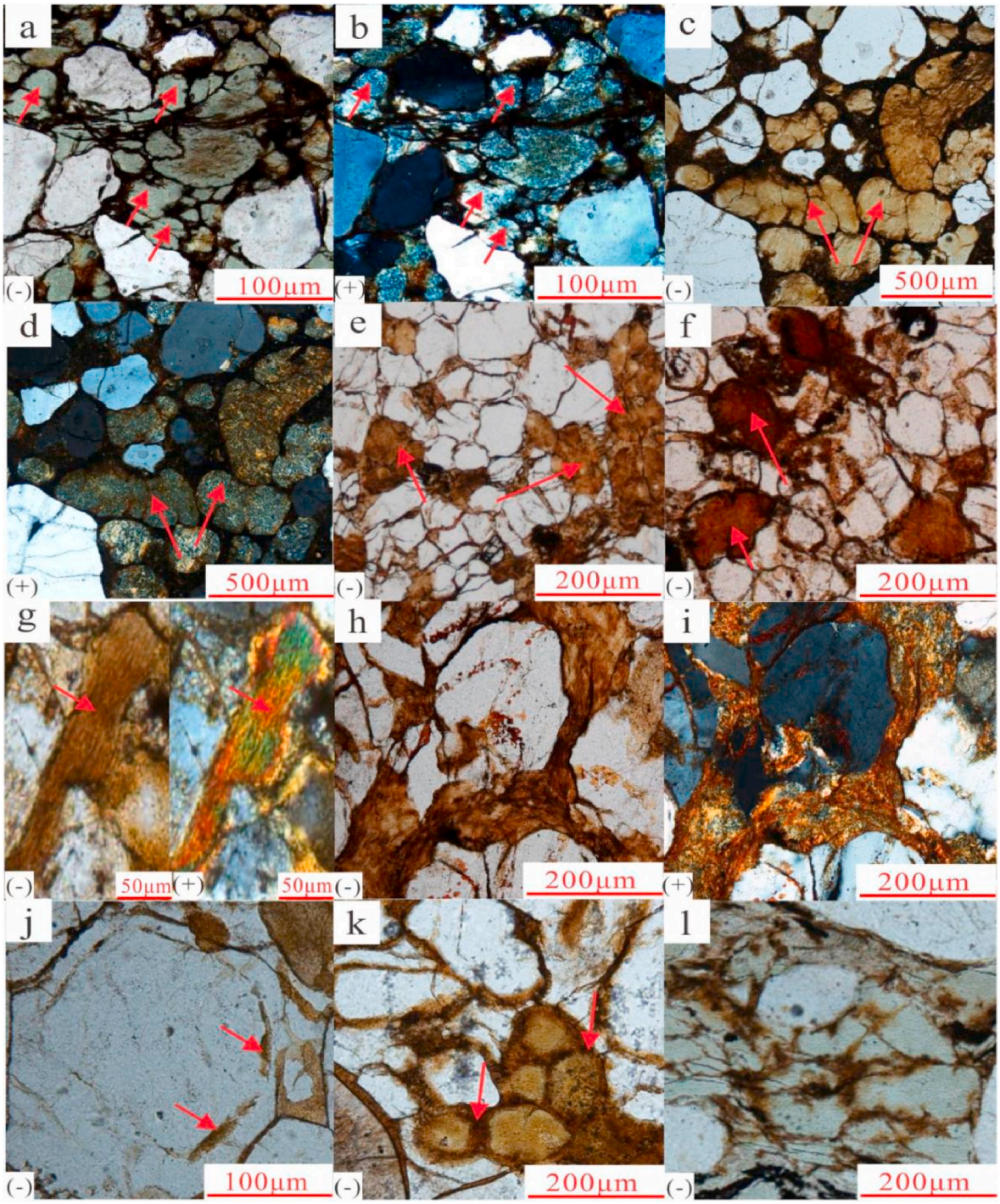

Fig. 3. Microscopic images of glauconites of the Qingbaikou System in the Longshan area. Notes: (a) and (b) Green granular glauconites (Ch Fm.); (c) and (d) Yellow-green granular glauconites (Ch Fm.); (e) Yellow-brown granular glauconites (Ch Fm.); (f) Detrital glauconites (Ch Fm.); (g) Pseudomorphic glauconites (mica pseudomorphic) (Xi Fm.); (h) and (i) Colloidal glauconites (Ch Fm.); (j) Colloidal glauconites existing between quartz overgrowth edges and quartz grains (Ch Fm.); (k) Halo-rimmed glauconites (Ch Fm.); (l) Pigment-infected glauconites (Ch Fm.); Xi Fm.-Xiamaling Formation; Ch Fm.-Changlongshan Formation.

3.3. Major oxide composition of glauconite

The chemical compositions of glauconite in the target layer of the study area are presented in Fig. 5 and Table 1.

The contents of K_2O, TFeO and SiO_2 of the five types of glauconites vary significantly (Table 1). From Type I to V, the K_2O content in the glauconite decreases sequentially, i.e., the K_2O content of Type I glauconites are the highest, and those of the Type V glauconites are the lowest, reflecting their decreasing maturity (Rudmin et al., 2017; Sánchez-Navas et al., 2008; Wigle and Compton, 2007; Roy Choudhury et al., 2021). Type I and II glauconites have relatively low TFeO content (less than 12%), while Type III, IV, and V glauconites have relatively high TFeO content (greater than 12%). In addition, the SiO_2 content of the Type I glauconite is the highest, and that of the Type V glauconite is the lowest. The differences in the contents of Al_2O_3 and MgO among the five types of glauconites are small.

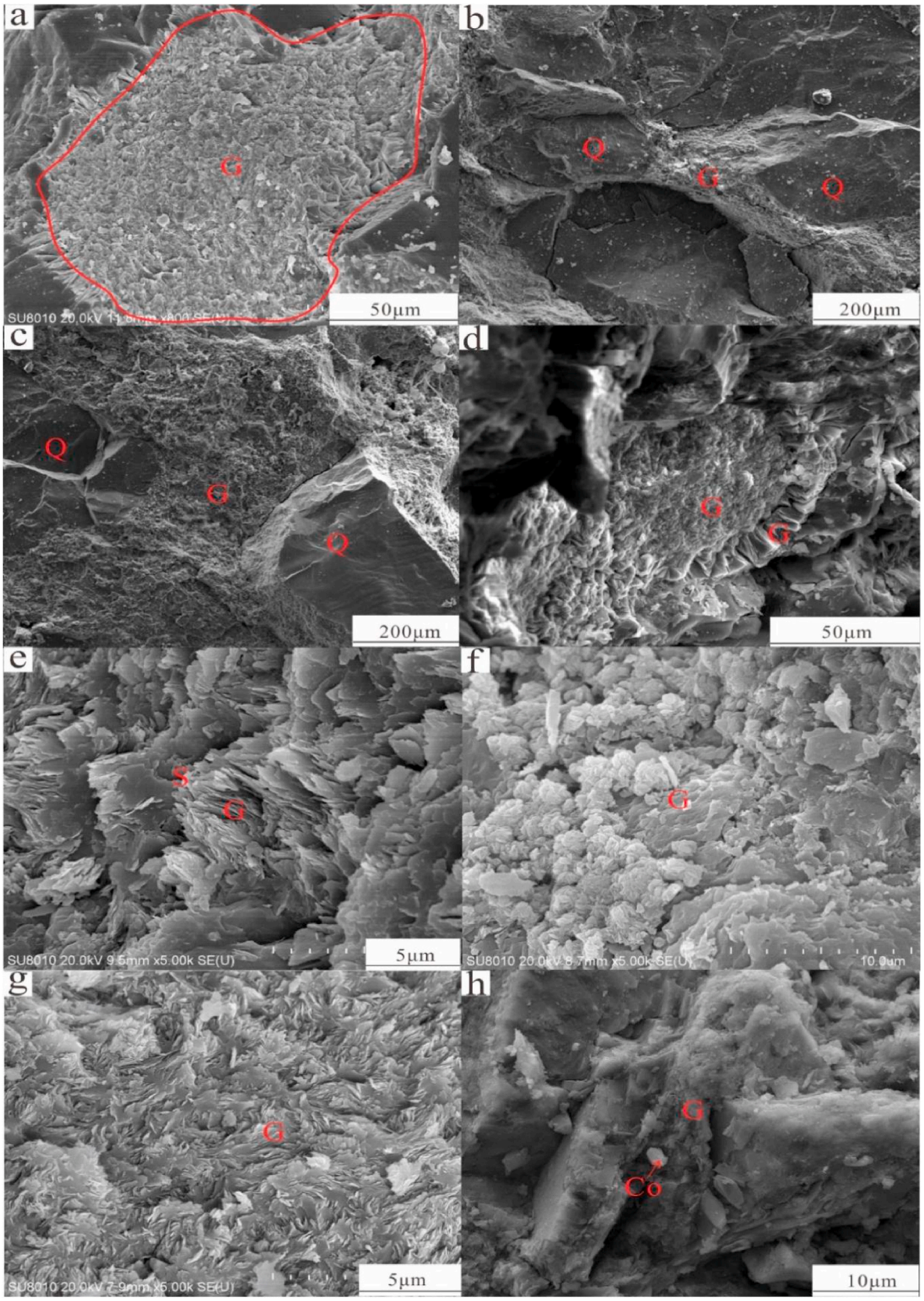

Fig. 4. Microscopic characteristics of the glauconites in the Longshan Area. Notes: (a) Granular glauconite (Ch Fm.); (b) Colloidal glauconite (Xi Fm.); (c) Cement-like glauconite (Ch Fm.); (d) Halo-rimmed glauconite (Ch Fm.); (e) Lamellar glauconite, symbiotic with siderite (Xi Fm.); (f) Curved lamellar glauconite (Ch Fm.); (g) Splintery glauconite (Ch Fm.); (h) Symbiotic glauconite and collophanite (Ch Fm.). Note: G-Glauconite; Q-Quartz; S-Siderite; Co-Collophanite; Xi Fm.-Xiamaling Formation; Ch Fm.-Changlongshan Formation.

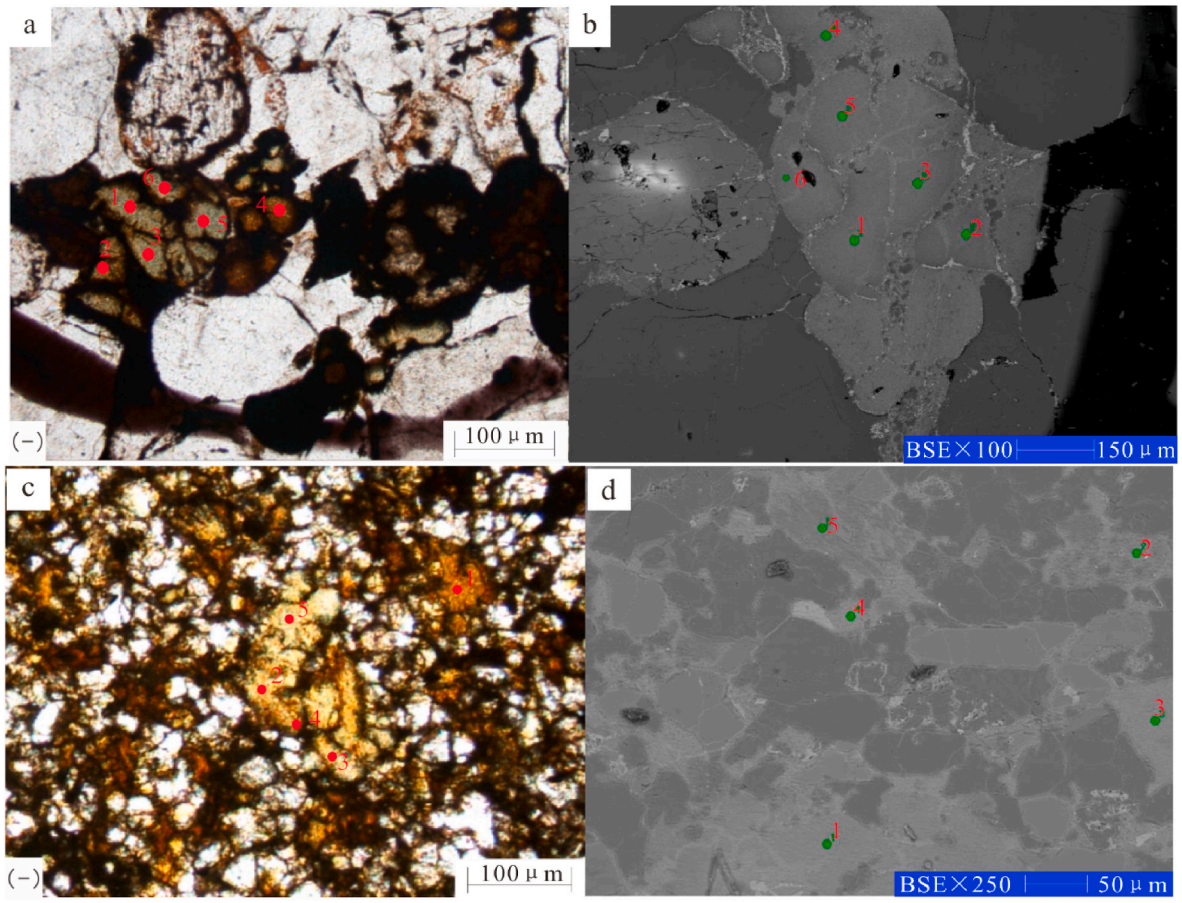

Fig. 5. Distribution of electron probe test dots in the glauconite samples. Notes: (a) and (b): Sample L7, Changlongshan Formation; (c) and (d): Sample X5, Xiamaling Formation).

3.4. Ionic structures of glauconite

In this study, the anion method (based on $O_{10}(OH)_2$) was adopted to calculate the ionic structures of the glauconite samples (Tang et al., 2016). The R^{3+} values of the glauconite samples range from 1.66 to 3.18, which are greater than 1.2 atoms; the M^{+} values of the Types I, II, and III glauconites are all greater than 0.4 atoms, which are consistent with the definition of glauconite given by the AIPEA (Adriaens et al., 2014; Baioumy and Boulis, 2012a; Banerjee et al., 2016a,b; López-Quirós et al., 2019). Ultimately, the glauconites in the study area are classified into three types according to their chemical formulae (Table 2):

Type I are the green granular glauconite

: $(K, Na, Ca)_{0.54\sim0.91}\left[Al, \left(Fe^{2+}, Fe^{3+}\right), Mg\right]_{0.88\sim1.97}(Si,\ Al)_4O_{10}(OH)_2$

• nH_2O;

Type II are the yellow – green granular glauconite

: $(K, Na, Ca)_{0.54\sim0.80}\left[Al, \left(Fe^{2+}, Fe^{3+}\right), Mg\right]_{0.77\sim2.36}(Si,\ Al)_4O_{10}(OH)_2$

• nH_2O;

Type III are the yellow – brown granular glauconite

: $(K, Na, Ca)_{0.39\sim0.57}\left[Al, \left(Fe^{2+}, Fe^{3+}\right), Mg\right]_{1.65\sim2.52}(Si,\ Al)_4O_{10}(OH)_2$

• nH_2O.

Type IV and Type V are the yellow-brown cement-like glauconite and the off-site glauconite, respectively. Due to alteration processes, their ionic structures no longer satisfy the basic definition of glauconite due to alteration. Therefore, their chemical formulas cannot be determined.

4. Discussion

4.1. Enrichment conditions of the Neoproterozoic glauconites

Glauconite forms over a long period of time and is characterized by low depositional rates, and a sufficient supply of cations such as iron, potassium, aluminum, silicon, and magnesium (Banerjee et al., 2016a,b; Mei et al., 2008; Strickler and Ferrell, 1990; Roy Choudhury et al., 2022a,b; Tounekti et al. al., 2021; Zhang et al., 2017a; Zhang et al., 2022; Zhang and Tutolo, 2021). The availability of iron controls the evolution of glauconite (Banerjee et al., 2012; Roy Choudhury et al., 2021), and the activity of irons is controlled by redox states (Fürsich et al., 2021). High silicon concentration is necessary for the formation of the early iron-rich glauconites (López-Quirós et al., 2019; Odin and Fullagar, 1988; Tang et al., 2017; Zhang and Tutolo, 2021). In addition, the silicon and potassium are derived from seawater with high silicon and terrigenous clasts content (Banerjee et al., 2016a,b; Guo et al., 2019; Roy Choudhury et al., 2022a,b; Wang et al., 2020; Zhang et al., 2016). Moreover, a suitable pH condition and an environment near the Fe redox interface are the most favorable conditions for the formation of glauconites (Tutolo et al., 2020; Zhang et al., 2017a; Zhang et al., 2022).

Feldspar-rich source rocks can provide various ions for glauconis in the Changlongshan and Xiamaling Formations. Trace elements such as La, Sc, Co, and Th can be used to indicate the types of source rocks. Specific relationship diagrams of different chemical elements were used to identify the tectonic setting and source rock types (Absar, 2021; Condie et al., 1991; Gu et al., 2002; McLennan, 1993; Wang et al., 2020; Zhang et al., 2020). In this study, different discriminant diagrams were drawn using 5 samples collected from the Changlongshan Formation

Table 1
Content of the major chemical components in different types of glauconite samples based on electron probe analysis (partial samples).

Type	Sample	SiO_2	Al_2O_3	TFeO	MgO	CaO	Na_2O	K_2O	P_2O_5	^{IV}Al	^{VIII}Al	R^{3+}	M^+
I	X1-3	56.61	21.26	7.21	4.30	1.72	0.03	8.80	0.07	0.35	1.26	2.06	0.85
	X5-5	51.12	30.08	4.73	3.00	2.24	0.19	8.65	0.00	0.73	1.54	2.08	0.88
	L7-1	58.62	22.92	3.61	4.33	1.99	0.07	8.46	0.00	0.31	1.39	1.98	0.82
	L7-2	59.59	21.91	3.45	4.73	1.74	0.04	8.47	0.07	0.26	1.36	1.99	0.80
	L7-3	58.91	22.10	3.88	4.47	2.02	0.06	8.48	0.08	0.28	1.36	1.98	0.83
	L7-5	58.11	22.22	4.76	4.43	2.00	0.04	8.42	0.03	0.32	1.34	2.01	0.82
	L7-6	59.33	21.23	5.26	4.50	0.76	0.25	8.68	0.00	0.25	1.34	2.04	0.78
	L15-1	55.14	24.96	4.68	3.76	1.79	0.02	9.62	0.02	0.47	1.41	2.02	0.91
	L15-2	55.07	25.18	4.94	3.56	1.77	0.03	9.40	0.03	0.48	1.42	2.02	0.89
	L15-3	55.49	25.37	4.08	3.76	1.66	0.06	9.54	0.03	0.47	1.44	2.01	0.90
	L10-1	58.10	24.07	4.96	3.61	0.00	0.04	9.21	0.01	0.33	1.46	2.06	0.75
	L10-3	57.93	24.23	4.85	3.81	0.00	0.05	9.11	0.03	0.34	1.46	2.07	0.74
II	X1-1	48.36	24.14	12.08	5.15	4.68	0.05	5.52	0.01	0.79	1.10	2.28	0.81
	X2-5	57.93	19.74	12.59	3.11	0.42	0.07	6.14	0.00	0.26	1.24	2.22	0.54
	X5-1	45.35	24.50	14.01	6.18	5.69	0.05	4.20	0.00	0.95	0.99	2.39	0.78
	X5-2	62.69	15.93	9.30	2.60	4.72	0.88	3.83	0.05	0.03	1.16	1.90	0.74
	X5-3	45.05	24.90	13.89	5.93	5.83	0.03	4.37	0.00	0.97	1.00	2.38	0.80
	L15-6	45.37	25.94	13.95	6.12	3.79	0.05	4.78	0.00	0.97	1.08	2.47	0.69
	L11-3	51.77	19.37	16.36	4.24	0.38	0.05	7.76	0.07	0.51	1.03	2.38	0.70
	L10-2	53.75	26.93	10.34	0.00	2.42	0.04	6.34	0.18	0.53	1.52	2.08	0.69
III	X2-1	52.20	19.82	19.31	4.01	0.46	0.10	4.10	0.00	0.52	1.04	2.52	0.39
	X2-2	47.72	21.83	20.83	3.51	0.67	0.10	5.34	0.01	0.74	1.02	2.57	0.53
	X2-3	49.70	20.74	19.86	4.81	0.53	0.14	4.20	0.03	0.65	1.00	2.60	0.42
	X2-6	50.09	20.89	19.39	5.00	0.54	0.13	3.95	0.00	0.64	1.01	2.60	0.39
	X2-7	54.83	19.05	15.60	4.12	0.45	0.08	5.85	0.01	0.38	1.10	2.36	0.53
	L12-1	48.56	18.47	23.57	4.90	0.77	0.15	3.57	0.03	0.66	0.83	2.69	0.39
	L12-2	53.75	18.97	16.35	4.16	0.50	0.12	6.10	0.05	0.43	1.06	2.38	0.57
	L12-4	49.44	16.56	23.24	5.37	0.77	0.16	4.34	0.13	0.59	0.76	2.65	0.46
IV	L9-1	51.59	15.97	23.74	5.12	0.55	0.41	2.48	0.14	0.49	0.80	2.67	0.31
	L11-1	37.93	20.96	28.84	8.48	0.41	0.12	3.11	0.15	1.26	0.53	3.18	0.34
	L11-2	38.58	20.77	29.44	7.98	0.33	0.13	2.72	0.06	1.22	0.55	3.18	0.29
	L15-5	42.98	25.89	15.66	7.48	5.17	0.06	2.71	0.05	1.10	0.95	2.58	0.61
	L12-3	48.24	18.21	22.68	6.76	0.99	0.21	2.81	0.09	0.70	0.77	2.76	0.35
V	L9-2	40.79	25.15	18.60	7.86	6.11	0.05	1.43	0.00	1.21	0.82	2.68	0.58
	L9-3	40.69	25.69	18.22	7.93	5.29	0.04	2.14	0.00	1.22	0.85	2.70	0.58
	L9-4	40.66	26.22	18.94	8.17	4.05	0.05	1.90	0.01	1.23	0.88	2.79	0.47
	L9-5	43.19	24.37	17.42	7.37	5.64	0.07	1.91	0.04	1.07	0.87	2.60	0.58
	L8-2	41.89	33.11	18.40	1.78	3.74	0.09	0.09	0.91	1.20	1.41	2.62	0.29
	L8-3	42.17	33.65	17.55	1.69	3.96	0.07	0.07	0.84	1.20	1.44	2.59	0.30
	L8-4	36.84	29.97	23.72	2.97	5.04	0.11	0.11	1.23	1.41	1.07	2.78	0.40

Notes: ^{IV}Al is tetrahedral site Al^{3+}; ^{VIII}Al is octahedral site Al^{3+}; R^{3+} is octahedral site cation; M^+ is interlayer cation.

and 2 samples from the Xiamaling Formation (Fig. 6). In the La–Th-Sc (Fig. 6a), Th–Co–Zr/10 (Fig. 6b) and Th-Sc-Zr/10 discriminant diagrams (Fig. 6c), most of the samples fall into the continental arc source region, while some samples from the Xiamaling Formation are located at the junction of the passive continental margin and the continental arc. Moreover, according to the La/Th–Hf discriminant diagram (Fig. 6d), the samples are located near the andesite arc and felsic source regions, indicating that the source rocks are a mixture of the andesite and felsic components. In the Co/Th–La/Sc diagram (Fig. 6e), the samples have moderate and relatively stable Co/Th values. The Co/Th values range from 0.63 to 2.63, with an average of 2.13. However, the La/Sc values are low, ranging from 1.00 to 3.14, with an average value of 1.85. The samples all fall between the felsic volcanic rock and andesite region. It reflects that the source rocks are a mixture of andesite and felsic. Therefore, the trace element provenance and source rocks (Fig. 6) of the Xiamaling and Changlongshan Formations have the tectonic background of continental island arcs, and the source rocks are both mixed andesite and felsic components, which can provide favorable source materials for the formation of glauconites.

The existence of multi-stage unconformities is beneficial to the supply of ions during the formation of glauconite. Previous studies have shown that the “Weixian Activity” between the Changlongshan and Xiamaling Formations and the “Qinyu Activity” between the Xiamaling and its overlying Mesoproterozoic Tieling Formation caused the formation of unconformities (Fig. 1) (Pan et al., 2013; Zhou et al., 2006; Zhu et al., 2012). Stromatolite limestones containing glauconite are well developed on the top of the Tieling Formation (Mei et al., 2008; Mei, 2018). In the Xiamaling Formation of North China, iron components and glauconites are well developed: the upper part are green and emerald green shales intercalated with thin layers of iron siltstones; the lower part are glauconite-bearing sandstones that contain siderite and pyrite lens; while iron-bearing glauconites and iron-cemented conglomerates are developed in the bottom. Lenticular iron ore or iron-bearing coarse sandstone is common and overlaid on top of conglomerate. In the Jixian Profile, siderite-bearing sandstones and 2 to 4 layers of intermediate-basic volcanic rock beds are developed in the Xiamaling Formation, and tuffs are also developed at the top (Guo et al., 2019; Qu et al., 2012). They provide the material for the enrichment of iron, magnesium and glauconites for the Changlongshan Formation. The multi-stage unconformities between the Tieling & Xiamaling and the Xiamaling & Changlongshan Formations have caused the iron- and glauconite-bearing sandstones, siltstones, shales and intermediate-basic volcanic rocks to suffer from long-term weathering. Moreover, various ion sources and substrate minerals are provided for the formation of glauconites in the Xiamaling and Changlongshan Formations.

In addition, granitic conglomerates and feldspar sandstones are developed at the bottom of the Changlongshan Formation (Fig. 7), in which the dissolution of the K-feldspar provides rich K^+ and substrate minerals for glauconites in the middle part of the Changlongshan Formation. The detrital glauconites developed in the Changlongshan Formation have good roundness, while the siltstones and argillaceous siltstones in the Xiamaling Formation develop large-scale glauconite cements (Zhang et al., 2020). It can be inferred that these round detrital glauconites are mainly formed after re-transportation and re-deposition

Table 2
Chemical formulas calculated by partial electron probe dots in the glauconite samples from the study area.

Type	Sample	Dot number	Chemical formulas
Type I granular glauconite	X-01	3	$(K_{0.72},Na_{0.00},Ca_{0.12})_{0.85}$ $[Al_{0.35}(Fe^{2+},Fe^{3+})_{0.39}Mg_{0.41}]_{1.15}(Si_{3.65},Al_{1.26})_4O_{10}(OH)_2\bullet nH_2O$
	X-05	5	$(K_{0.71},Na_{0.02},Ca_{0.15})_{0.88}$ $[Al_{0.73}(Fe^{2+},Fe^{3+})_{0.25}Mg_{0.29}]_{1.27}(Si_{3.27},Al_{1.54})_4O_{10}(OH)_2\bullet nH_2O$
	L-07	1	$(K_{0.68},Na_{0.01},Ca_{0.13})_{0.82}$ $[Al_{0.31}(Fe^{2+},Fe^{3+})_{0.19}Mg_{0.41}]_{0.91}(Si_{3.69},Al_{1.39})_4O_{10}(OH)_2\bullet nH_2O$
		3	$(K_{0.68},Na_{0.00},Ca_{0.12})_{0.80}$ $[Al_{0.26}(Fe^{2+},Fe^{3+})_{0.18}Mg_{0.44}]_{0.88}(Si_{3.74},Al_{1.36})_4O_{10}(OH)_2\bullet nH_2O$
		5	$(K_{0.68},Na_{0.01},Ca_{0.14})_{0.83}$ $[Al_{0.28}(Fe^{2+},Fe^{3+})_{0.20}Mg_{0.42}]_{0.91}(Si_{3.72},Al_{1.36})_4O_{10}(OH)_2\bullet nH_2O$
	L-15	1	$(K_{0.68},Na_{0.00},Ca_{0.14})_{0.82}$ $[Al_{0.32}(Fe^{2+},Fe^{3+})_{0.25}Mg_{0.42}]_{0.99}(Si_{3.68},Al_{1.34})_4O_{10}(OH)_2\bullet nH_2O$
		2	$(K_{0.70},Na_{0.03},Ca_{0.05})_{0.78}$ $[Al_{0.25}(Fe^{2+},Fe^{3+})_{0.28}Mg_{0.42}]_{0.95}(Si_{3.75},Al_{1.34})_4O_{10}(OH)_2\bullet nH_2O$
		3	$(K_{0.78},Na_{0.00},Ca_{0.12})_{0.91}$ $[Al_{0.47}(Fe^{2+},Fe^{3+})_{0.25}Mg_{0.36}]_{1.08}(Si_{3.53},Al_{1.41})_4O_{10}(OH)_2\bullet nH_2O$
	L-10	1	$(K_{0.77},Na_{0.00},Ca_{0.12})_{0.89}$ $[Al_{0.48}(Fe^{2+},Fe^{3+})_{0.26}Mg_{0.34}]_{1.08}(Si_{3.52},Al_{1.42})_4O_{10}(OH)_2\bullet nH_2O$
		3	$(K_{0.77},Na_{0.01},Ca_{0.11})_{0.90}$ $[Al_{0.47}(Fe^{2+},Fe^{3+})_{0.22}Mg_{0.36}]_{1.04}(Si_{3.53},Al_{1.44})_4O_{10}(OH)_2\bullet nH_2O$
	L-02	1	$(K_{0.74},Na_{0.00},Ca_{0.00})_{0.75}$ $[Al_{0.33}(Fe^{2+},Fe^{3+})_{0.26}Mg_{0.34}]_{0.93}(Si_{3.67},Al_{1.46})_4O_{10}(OH)_2\bullet nH_2O$
		3	$(K_{0.73},Na_{0.01},Ca_{0.00})_{0.74}$ $[Al_{0.34}(Fe^{2+},Fe^{3+})_{0.26}Mg_{0.36}]_{0.96}(Si_{3.66},Al_{1.46})_4O_{10}(OH)_2\bullet nH_2O$
		5	$(K_{0.47},Na_{0.01},Ca_{0.33})_{0.81}$ $[Al_{0.79}(Fe^{2+},Fe^{3+})_{0.67}Mg_{0.51}]_{1.97}(Si_{3.21},Al_{1.10})_4O_{10}(OH)_2\bullet nH_2O$
Type II granular glauconite	X-01	1	$(K_{0.51},Na_{0.01},Ca_{0.03})_{0.54}$ $[Al_{0.26}(Fe^{2+},Fe^{3+})_{0.68}Mg_{0.30}]_{1.24}(Si_{3.74},Al_{1.24})_4O_{10}(OH)_2\bullet nH_2O$
	X-02	5	$(K_{0.36},Na_{0.01},Ca_{0.41})_{0.78}$ $[Al_{0.95}(Fe^{2+},Fe^{3+})_{0.79}Mg_{0.62}]_{2.36}(Si_{3.05},Al_{0.99})_4O_{10}(OH)_2\bullet nH_2O$
	X-05	1	$(K_{0.31},Na_{0.11},Ca_{0.32})_{0.74}$ $[Al_{0.03}(Fe^{2+},Fe^{3+})_{0.49}Mg_{0.25}]_{0.77}(Si_{3.97},Al_{1.16})_4O_{10}(OH)_2\bullet nH_2O$
		2	$(K_{0.37},Na_{0.00},Ca_{0.42})_{0.80}$ $[Al_{0.97}(Fe^{2+},Fe^{3+})_{0.78}Mg_{0.59}]_{2.35}(Si_{3.03},Al_{1.00})_4O_{10}(OH)_2\bullet nH_2O$
		3	$(K_{0.41},Na_{0.01},Ca_{0.27})_{0.69}$ $[Al_{0.97}(Fe^{2+},Fe^{3+})_{0.78}Mg_{0.61}]_{2.36}(Si_{3.03},Al_{1.08})_4O_{10}(OH)_2\bullet nH_2O$
	L-15	6	$(K_{0.67},Na_{0.01},Ca_{0.03})_{0.70}$ $[Al_{0.51}(Fe^{2+},Fe^{3+})_{0.92}Mg_{0.43}]_{1.86}(Si_{3.49},Al_{1.03})_4O_{10}(OH)_2\bullet nH_2O$
	L-10	2	$(K_{0.52},Na_{0.01},Ca_{0.17})_{0.69}$ $[Al_{0.53}(Fe^{2+},Fe^{3+})_{0.56}Mg_{0.00}]_{1.09}(Si_{3.47},Al_{1.52})_4O_{10}(OH)_2\bullet nH_2O$
Type III granular glauconite	X-02	1	$(K_{0.35},Na_{0.01},Ca_{0.03})_{0.39}$ $[Al_{0.52}(Fe^{2+},Fe^{3+})_{1.08}Mg_{0.40}]_{1.99}(Si_{3.48},Al_{1.04})_4O_{10}(OH)_2\bullet nH_2O$
		2	$(K_{0.47},Na_{0.01},Ca_{0.05})_{0.53}$ $[Al_{0.74}(Fe^{2+},Fe^{3+})_{1.19}Mg_{0.36}]_{2.29}(Si_{3.26},Al_{1.02})_4O_{10}(OH)_2\bullet nH_2O$
		3	$(K_{0.36},Na_{0.02},Ca_{0.04})_{0.42}$ $[Al_{0.65}(Fe^{2+},Fe^{3+})_{1.12}Mg_{0.48}]_{2.25}(Si_{3.35},Al_{1.00})_4O_{10}(OH)_2\bullet nH_2O$
		6	$(K_{0.34},Na_{0.02},Ca_{0.04})_{0.39}$ $[Al_{0.64}(Fe^{2+},Fe^{3+})_{1.09}Mg_{0.50}]_{2.23}(Si_{3.36},Al_{1.01})_4O_{10}(OH)_2\bullet nH_2O$
		7	$(K_{0.49},Na_{0.01},Ca_{0.03})_{0.53}$ $[Al_{0.38}(Fe^{2+},Fe^{3+})_{0.86}Mg_{0.41}]_{1.65}(Si_{3.62},Al_{1.10})_4O_{10}(OH)_2\bullet nH_2O$
	L-12	1	$(K_{0.31},Na_{0.02},Ca_{0.06})_{0.39}$ $[Al_{0.66}(Fe^{2+},Fe^{3+})_{1.35}Mg_{0.50}]_{2.52}(Si_{3.34},Al_{0.83})_4O_{10}(OH)_2\bullet nH_2O$
		2	$(K_{0.52},Na_{0.02},Ca_{0.04})_{0.57}$ $[Al_{0.43}(Fe^{2+},Fe^{3+})_{0.91}Mg_{0.41}]_{1.75}(Si_{3.57},Al_{1.06})_4O_{10}(OH)_2\bullet nH_2O$
		4	$(K_{0.38},Na_{0.02},Ca_{0.06})_{0.46}$ $[Al_{0.59}(Fe^{2+},Fe^{3+})_{1.34}Mg_{0.55}]_{2.48}(Si_{3.41},Al_{0.76})_4O_{10}(OH)_2\bullet nH_2O$

of the glauconite cements that well-developed in the Xiamaling Formation.

In summary, the Xiamaling Formation in the study area has experienced intense volcanic activities and has widely-distributed intermediate-basic volcanic rock which can provide the source of iron and magnesium components, and large-scale glauconite-bearing shales and sandstones (Zhang et al., 2020). Moreover, the long-term weathering after the deposition of the Xiamaling and Tieling Formations, and dissolution of K-feldspar in the lower part of the Changlongshan Formation provided various ion sources for the formation of autochthonous glauconites, and it also has a certain affinity with the detrital glauconite. In addition, during the Precambrian period, the content of Mg^{2+} in seawater was relatively high (Banerjee et al., 2016a,b; Tang et al., 2016; Zhang et al., 2017b), which provided the magnesium component required for the development of glauconites.

4.2. Composite origin and evolution of different types of glauconite

The most widely accepted theories of glauconite formation include layered lattice, grain verdissement, pseudomorphic replacement, authigenic cementation and alteration theories (Amorosi et al., 2007; Banerjee et al., 2015; Bansal et al., 2018; Burst, 1958; Eder et al., 2007; Fernández-Landero and Fernández-Landero and Fernández-Caliani, 2021; Hegab et al., 2016; Jafarzadeh et al., 2020; Mandal et al., 2020; López-Quirós et al., 2019; Mandal et al., 2022; Odin and Matter, 1981; Roy Choudhury et al., 2022a,b; Zhang et al., 2016). Cross-plots of different oxide content in the glauconite show different evolution trends, which helps assess the origin mechanism of the glauconite (Tang et al., 2016; Zhang, 2018). Fig. 8 is a covariation diagram based on the content of the K_2O and TFeO in the glauconite, developed over different time periods and in different regions (Banerjee et al., 2015; Chen, 1980; Mandal et al., 2020; Sánchez-Navas et al., 2008; Wang et al., 2020; Xu et al., 2010; Yang et al., 2016; Zhang, 2018). There are significant differences in the genesis of the glauconites that formed in the Phanerozoic and Precambrian (Fig. 8). The former conforms to the layered lattice theory or the grain verdissement theory, while the latter conforms to the pseudomorphic replacement theory.

Table 1 and Fig. 9 show the covariation relationship between the content of different chemical components in Neoproterozoic glauconites, Longshan area. Type I or the green granular glauconites exhibit high K_2O, Al_2O_3, SiO_2 and MgO content, and low TFeO content (Table 1, Fig. 9). The K_2O content of the glauconite corresponds to 'evolved' and 'highly evolved' stages of maturity (Amorosi, 1997; Odin and Matter, 1981; Mandal et al., 2020). High K_2O content can be used to distinguish the minerals from illites, while the ferric illite can be distinguished by low TFeO and high Al_2O_3 content (Banerjee et al., 2008; Dasgupta et al., 1990; Deb and Fukuoka, 1998; Mandal et al., 2020; Odin and Matter, 1981). All the sample data points of the Type I glauconite occupy the field of ferric illite in the K_2O vs. TFeO cross plot by Odin and Matter (1981) (Fig. 9a). The K_2O content in the Type I glauconite increases with the increase of the SiO_2 content (Fig. 9b). Type I glauconites show an

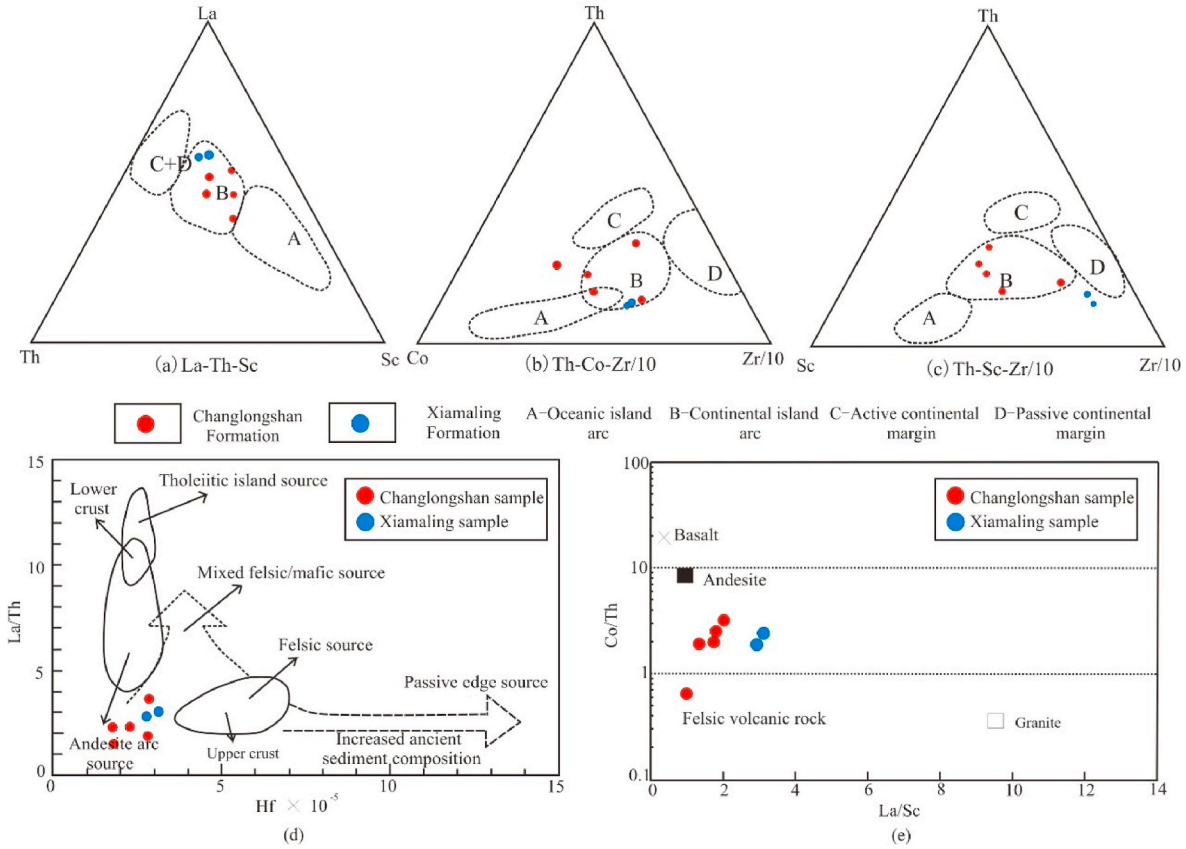

Fig. 6. Discrimination diagram of trace element source regions and source rocks of Changlongshan and Xiamaling Formations in Longshan area (Base map according to Condie et al., 1991).

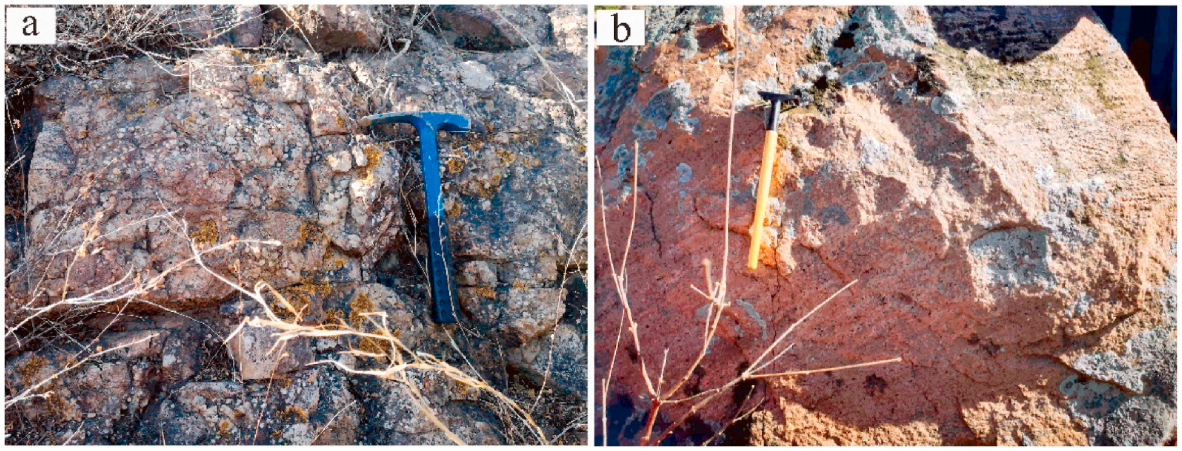

Fig. 7. Characteristics of felsic conglomerate and coarse feldspar sandstone in the lower Changlongshan Formation in Longshan area. a. Felsic conglomerate, the gravels are mainly composed of granite, K-feldspar and quartz; b. Coarse feldspar sandstones with cross-bedding.

evolutionary trend in which the K_2O content remains constant with the variable TFeO content (Fig. 9a). It follows a similar trend to other records of the Precambrian glauconites (Fig. 8), in accord with the 'pseudomorphic replacement' theory involving the supply of excess K^+ and Si^{4+} in the pore water by the dissolution of K-feldspar (Bansal et al., 2018; Jafarzadeh et al., 2020; López-Quirós et al., 2019; Mandal et al., 2022; Roy Choudhury et al., 2021). The positive correlation between K_2O and Al_2O_3 content (Fig. 9c) implies that K and Al incorporated into glauconite structures simultaneously (Dasgupta et al., 1990; Baioumy and Boulis, 2012b; Banerjee et al., 2012a, b; Eder et al., 2007; Tounekti et al., 2021). Combined with the microphotoes under the thin sections (Fig. 3), the parent substrate of the glauconite is quartz or feldspar. Pseudomorphic replacement of quartz and feldspar by glauconites is evident for the Type I glauconites. According to the previous analysis, dissolution and weathering of the K-feldspar from the intermediate-basic volcanic rocks of the Xiamaling Formation (Zhang et al., 2022) and felsic conglomerate & arkose in the lower part of the Changlongshan Formation (Fig. 7) resulted in high K^+ and Si^{4+} concentrations in the pore water (Banerjee et al., 2015; Stille and Clauer, 1994; Zhang et al., 2020). The Type I glauconites are formed by the dissolution and replacement of the original K-feldspar or quartz substrate at a constant K_2O and a variable TFeO content. The formation

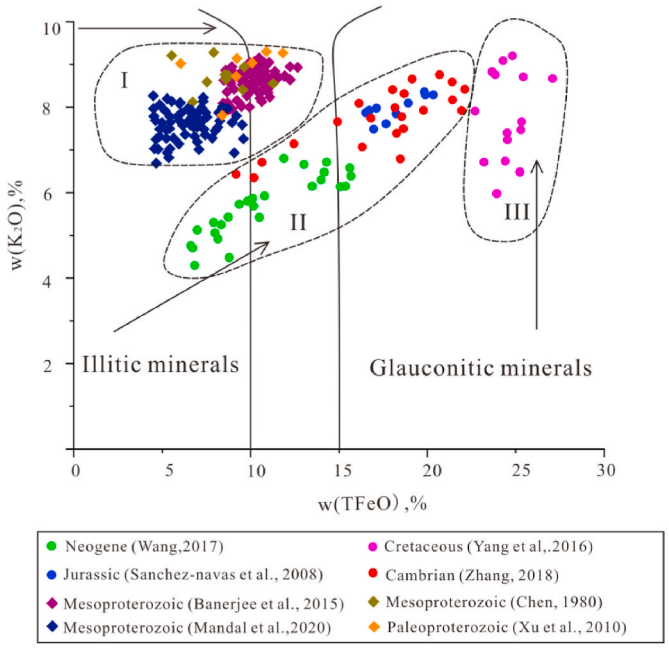

Fig. 8. Covariation diagram of K_2O and TFeO in the glauconite samples at different times. Fields of illitic and glauconitic minerals are after Odin and Matter (1981). Notes: Region I-samples conform to the pseudomorphic replacement theory; Region II- samples conform to the layered lattice theory; Region III- samples conform to the grain verdissement theory. Evolutionary trends in case of three genesis theories are presented by black line arrows.

process of the Type I glauconite can be summarized as follows. In the early stage, the glauconites were formed in discrete tiny patches in the early dissolute micropores or cleavage of the substrate in the form of euhedral crystals in the high K^+ and Si^{4+} content pore water (Fig. 10a) (Banerjee et al., 2008; Zhang et al., 2016). The pigment-infected glauconites in the tiny secondary pores or fractures in the substrate particles are the products of this period in this study. Subsequently, these tiny glauconite patchs slowly merge to form glauconite pellet symbiotic with the substrate grains, until the entire substrate particles are engulfed by the yellow-green pellet with high K_2O and high Al_2O_3 content (Figs. 10a and 11). As glauconization progressed, Fe ions gradually replace Al ions in the octahedral site due to the weak negative correlation (Fig. 9d). Then, more and more Fe^{2+} are incorporated into the crystal lattices of glauconite (Fig. 9a), and the color gradually changed from yellow-green to green, and eventually, the Type I green granular glauconites are form (Figs. 10a and 11).

The K_2O content of the Type II yellow-green granular glauconite is lower than that of the Type I glauconite (Table 1). The content of K_2O is roughly positively proportional to the content of TFeO (Fig. 9a). The relationship between the content of K_2O and Al_2O_3 is poor. Most of the sample data of the Types II glauconites occupy the field of 'compositional gap' in the K_2O vs. Fe_2O_3 cross plot by Odin and Matter (1981), and exhibits a general evolutional trend with layer lattice theory in the K_2O vs. TFeO cross plot by Odin and Matter (1981) (Figs. 8 and 9a). Layer lattice theory (Burst, 1958) envisages origin and evolution of glauconites by the incorporation of Fe and K ions simultaneously into the lattice of clay minerals like high alumina smectite, illite or degraded mica. From the micrographs (Fig. 3c,d,g), it can be inferred that the parent substrate of the Type II glauconites is mica or quartz. For the glauconites evolved from quartz substrate, the quartz may be replaced by high alumina smectite and other clay minerals in the early stage. Then, both the Fe and K ions are incorporated into the clay mineral lattices, and glauconite is formed. The evolution trend of the Type II glauconite is characterized by the simultaneous increase of K and Fe ions in its internal structures (Fig. 9a).

The content of K_2O in the Type III yellow-brown granular glauconites ranges from 3.57% to 6.01%. However, its TFeO content is relatively high (15.6%~23.57%). The K_2O content for most of the Type III samples decreases with increasing TFeO content (Fig. 9a), and it is inconsistent with the four genesis mechanism theories proposed previously. The yellow-brown granular glauconites form by 'alteration'. Here, the total iron content in the glauconite is relatively higher, while the potassium content is relatively lower. The Fe^{2+} are converted into Fe^{3+} ions, which in turn causes the color of the glauconite to change from green to yellowish-brown (Fig. 12). However, the morphology of glauconite is still the same as that of the surrounding quartz grains, and the residual optical characteristics of the quartz grains are also faintly visible under orthogonal light. This indicates that the Type III glauconites are formed due to the oxidative alteration of the Types I or II glauconites at a later stage, but its chemical structure still meets the definition of glauconite. Types I or II glauconites have undergone an oxidative transformation process and absorbed a large amount of Fe^{3+}, the contents of K^+ and Fe^{2+} decreased, the color changed to yellow-brown, and the Type III glauconites are formed finally (Figs. 10b and 11).

Type IV or the yellow-brown colloidal glauconites are mainly developed between quartz grains, and they include rimmed and pigment-infested glauconites. Zhang et al. (2016) proposed that the colloidal glauconites can be explained by the "autogenous cementation theory". During the diagenetic process, sufficient K, Si, Al and Fe ions in the weakly reducing and alkaline pore water environment favours the precipitation of authigenic glauconite (Tang et al., 2017a; Rudmin et al., 2017; Bansal et al., 2018). The colloidal glauconites found in the study area usually have a yellowish-brown or dark-brown color, and the concentrations of the K^+ and Si^{4+} are less than 0.3 and 3.0, respectively, which does not meet the definition of glauconite (Odin and Fullagar, 1988; Tang et al., 2017). Glauconite can be easily converted to limonite or goethite under certain oxidizing conditions, and goethite can be converted to hematite upon dehydration (Rudmin et al., 2017; Sánchez-Navas et al., 2008). Therefore, the cement-like yellow-brown and dark-brown cement-like "glauconites" maybe the iron oxide transformed by oxidation of glauconite in the late stage. The evolution of Type IV glauconites are (Fig. 13): In the pores between quartz grains, flocculent or speckled glauconite components are precipitated first; then, the speckles gradually aggregated and developed into green mature colloidal glauconites. In the Jixian area of Tianjin, most samples of this type of glauconites have not been oxidized and still appear green. However, the colloidal glauconites in the Longshan area have undergone strong oxidation, and most of them appear yellowish brown. The study found that the loss of K^+ in the colloidal glauconites was serious, and the yellowish brown color shows the ratio of Fe^{2+}/Fe^{3+} also decreased significantly (Harder, 1980; Hower, 1961; Sánchez-Navas et al., 2008). Therefore, most of the colloidal glauconites in the study area no longer meet the defined structures of glauconite, and have become the iron oxides of glauconite (Fig. 13). The formation processes of colloidal glauconites developed in the secondary enlarged edges of quartz and halo-rimmed glauconites are also similar. The former formed earlier than the secondary overgrowth of quartz. For halo-rimmed edge glauconites, they were formed by the growth of glauconite microparticles in the pore water along the surfaces of the early glauconite grains as the shell.

The Type V detrital granular glauconites are dark brown in color, and rounded or oval in shape (Fig. 3f). They were mainly formed in the Changlongshan Formation and are allochthonous glauconites. Zhang et al. (2020) proved that these granular glauconites were genetically related to the early glauconites developed in the early Xiamaling Formation, in which a large area of colloidal or mica pseudomorphic glauconites were found (Fig. 14). The areas of the continuous distributed glauconites are much larger than the surrounding quartz grains. As above analysis, the Xiamaling Formation suffering from long-term weathering provided a large amount of terrigenous detrital sources for the Changlongshan Formation (Zhang et al., 2020). It was inferred that

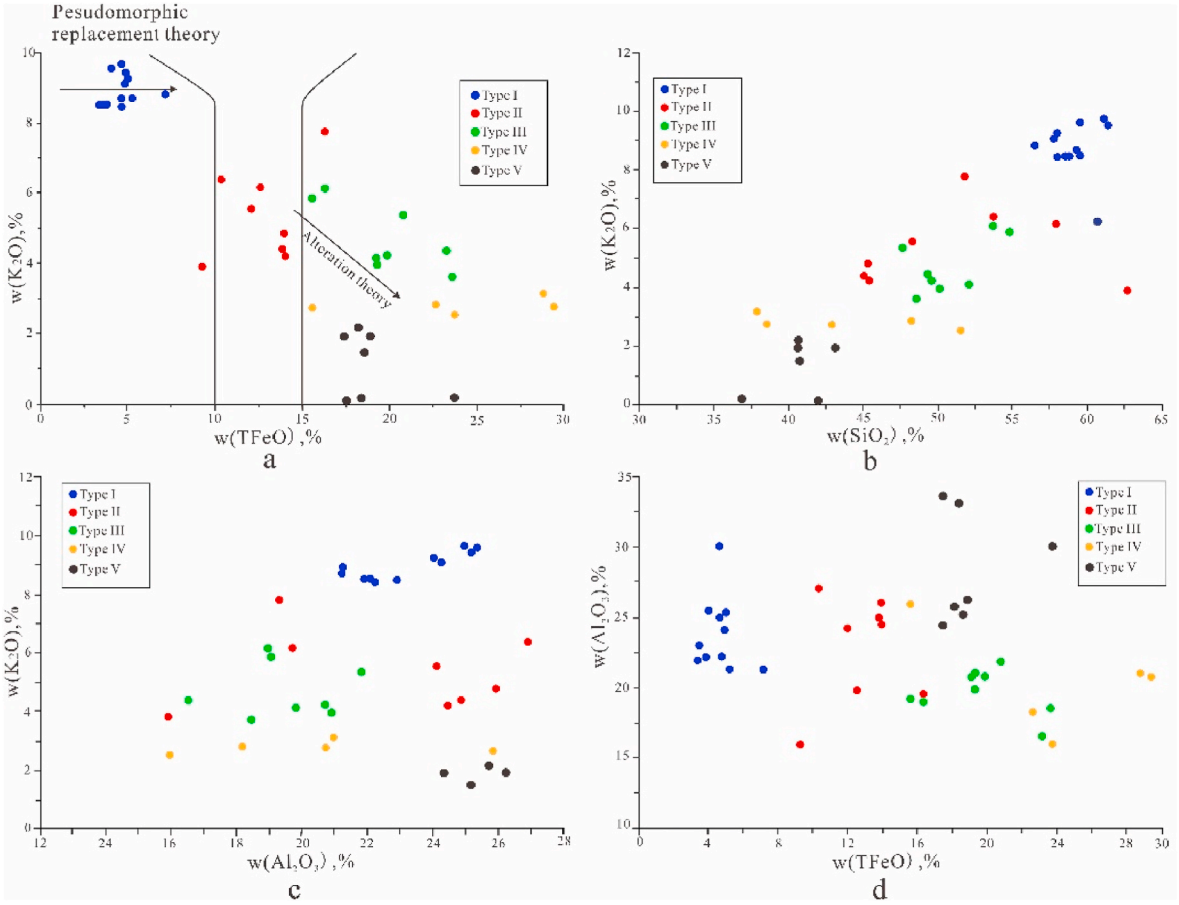

Fig. 9. Relationship between different mineral components in the glauconite samples from the Qingbaikou System in the Longshan area. Notes: (a) Cross-plot of K_2O vs. TFeO (total iron); (b) Cross-plot of K_2O vs. SiO_2; (c) Cross-plot of K_2O vs. Al_2O_3; (d) Cross-plot of Al_2O_3 vs. TFeO.

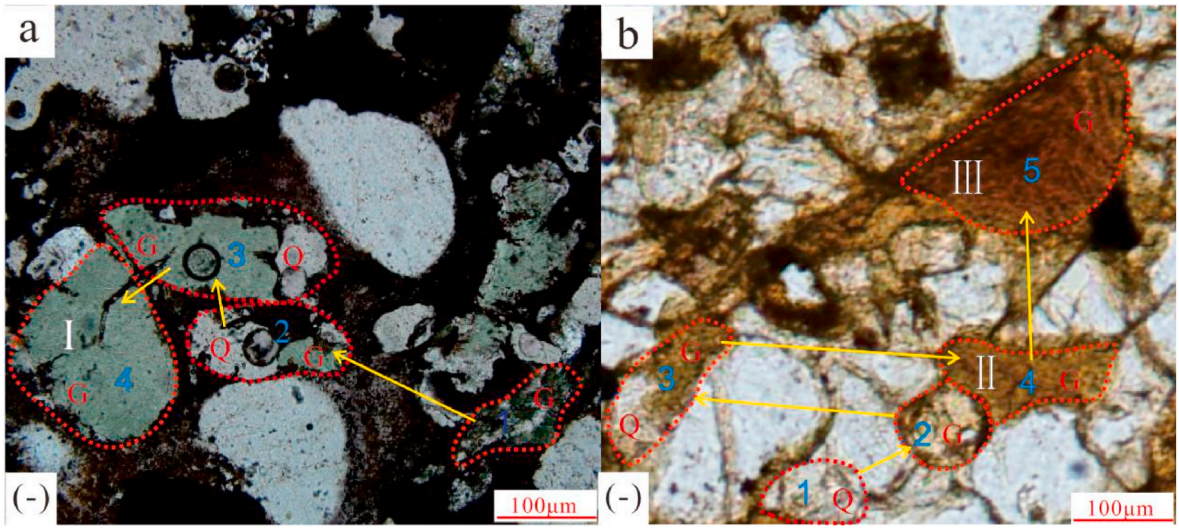

Fig. 10. Schematic diagram of the development process of granular glauconites (Changlongshan Formation). The numbers 1, 2, 3 and 4 represent different stages of glauconite development: 1- In the early stage, the glauconites were formed in discrete tiny patches; 2- Tiny glauconite patches merged slowly; 3-Glauconites continued to develop and almost engulfed the entire quartz substrate; 4- Quartz particles are completely transformed into glauconite particles; 5-Glauconites underwent the oxidative transformation process.

these contiguous glauconites were stirred up, re-transported, abrased and re-deposited by strong current in the later stage to form allochthonous detrital granular glauconites with better roundness. Most of the detrital glauconites in the study area appear dark brown, indicating that they have undergone strong oxidation during transportation. Electron probe analysis also showed that they no longer have the chemical compositions of glauconite. On the whole, the detrital granular glauconites belong to the composite origin of “authigenic cementation” or

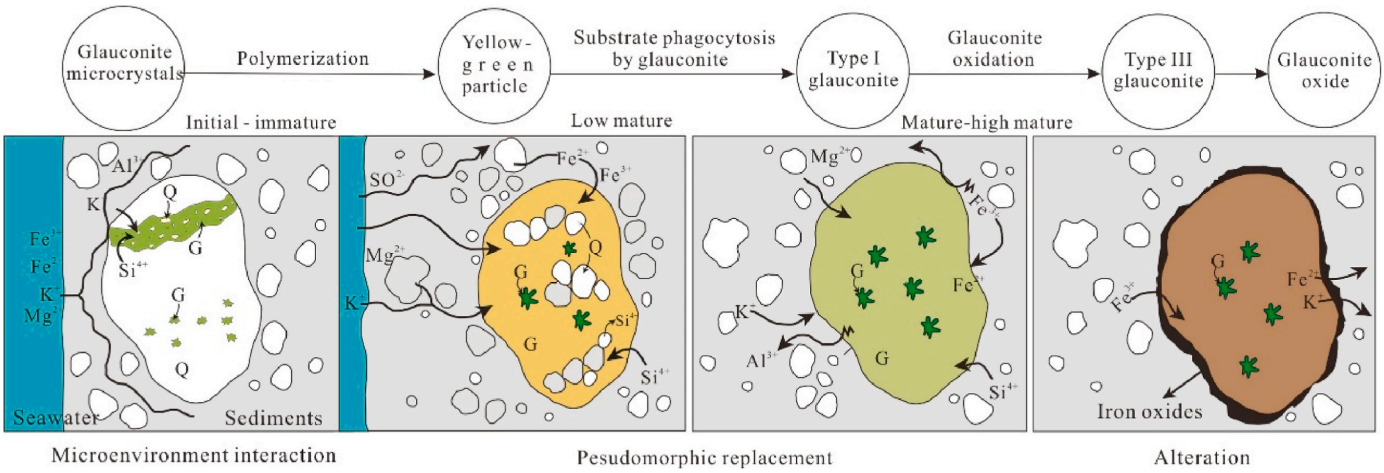

Fig. 11. Evolution mode of the autochthonous granular glauconites of Qingbaikou System in Longshan area. Note: G-glauconite, Q-quartz.

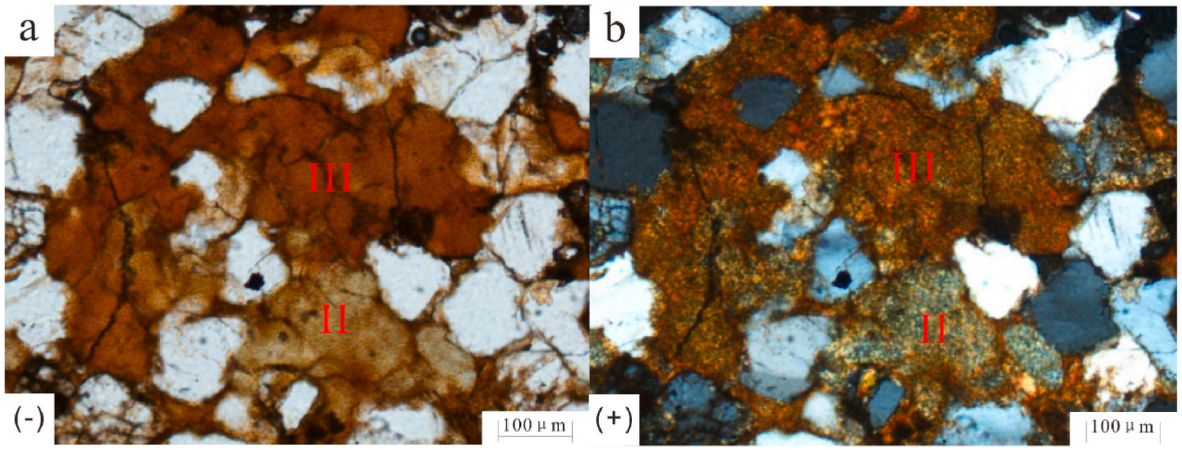

Fig. 12. Comparison of developmental characteristics of Types II and III granular glauconites (Changlongshan Formation). Type II is yellow-green, and Type III is yellow-brown. They have similar occurrence morphology.

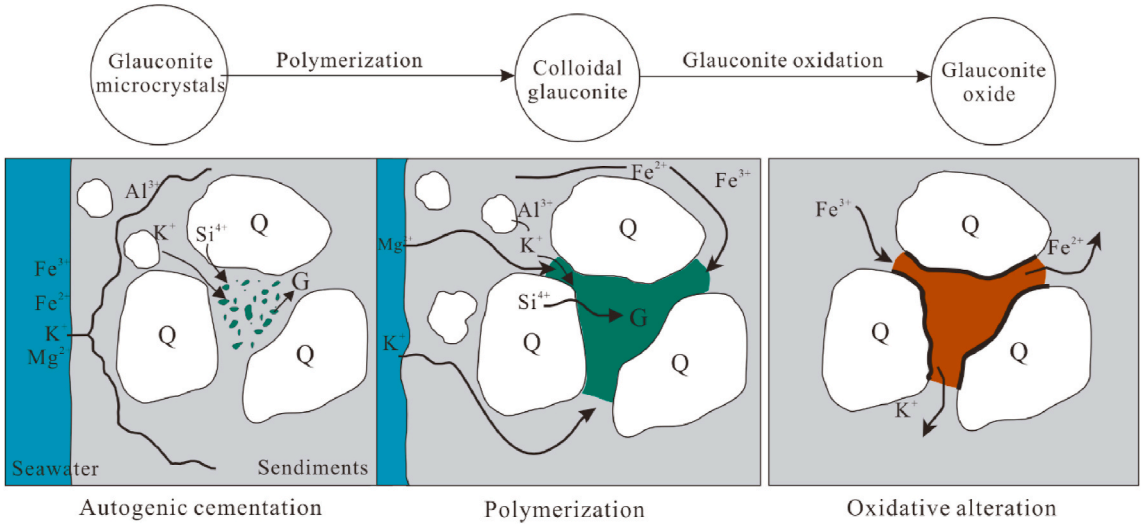

Fig. 13. Evolution mode of the autochthonous colloidal glauconites of the Qingbaikou System in the Longshan area. Notes: G-glauconite; Q-quartz.

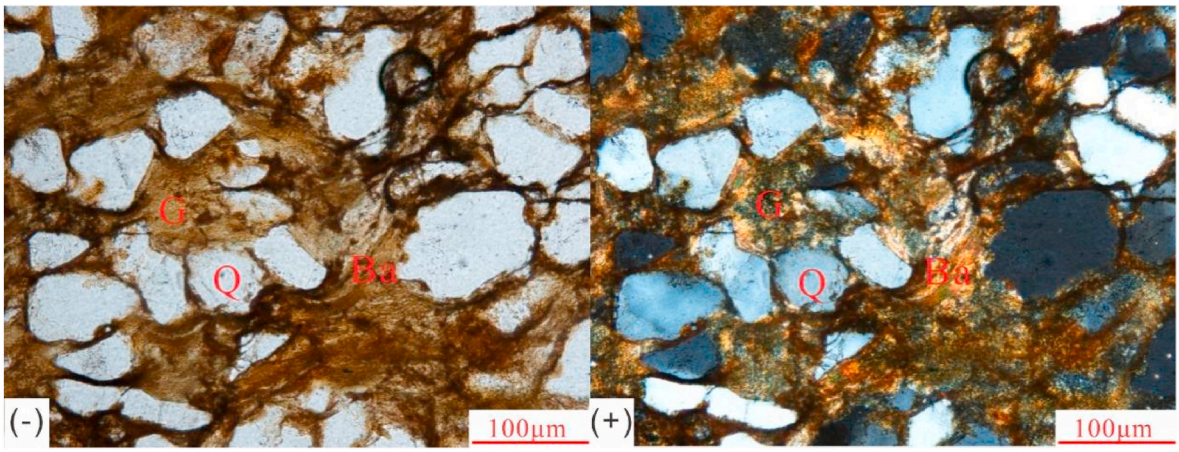

Fig. 14. Colloidal and mica pseudomorphic glauconites of the Xiamaling Formation in the Longshan area. Notes: G-Glauconite; Q-Quartz; Ba-Mica-altered glauconite.

"layered lattice" and later re-transportation and re-deposition.

4.3. Implication in depositional environment and diagenesis of the Neoproterozoic glauconites

The enrichment of glauconite requires suitable climate and sedimentary conditions, and the existence of authigenic glauconite can be used to analyze the sequence stratigraphic framework and restore the sedimentary environment (Amorosi et al., 2012; Baioumy and Boulis, 2012b; Ding, 1991; López-Quirós et al., 2019; Mandal et al., 2020; Roy Choudhury et al., 2022a,b). During the Precambrian period, the sea level was relatively high, and most of the glauconites were formed in a temperate-subtropical climate environment (Tang et al., 2017; Zhang et al., 2022). Glauconites are distributed across cratons, and their formation is related to the rising sea-level and slow rates of deposition on the continental shelf (Banerjee et al., 2015; Chen et al., 2014; Tutolo

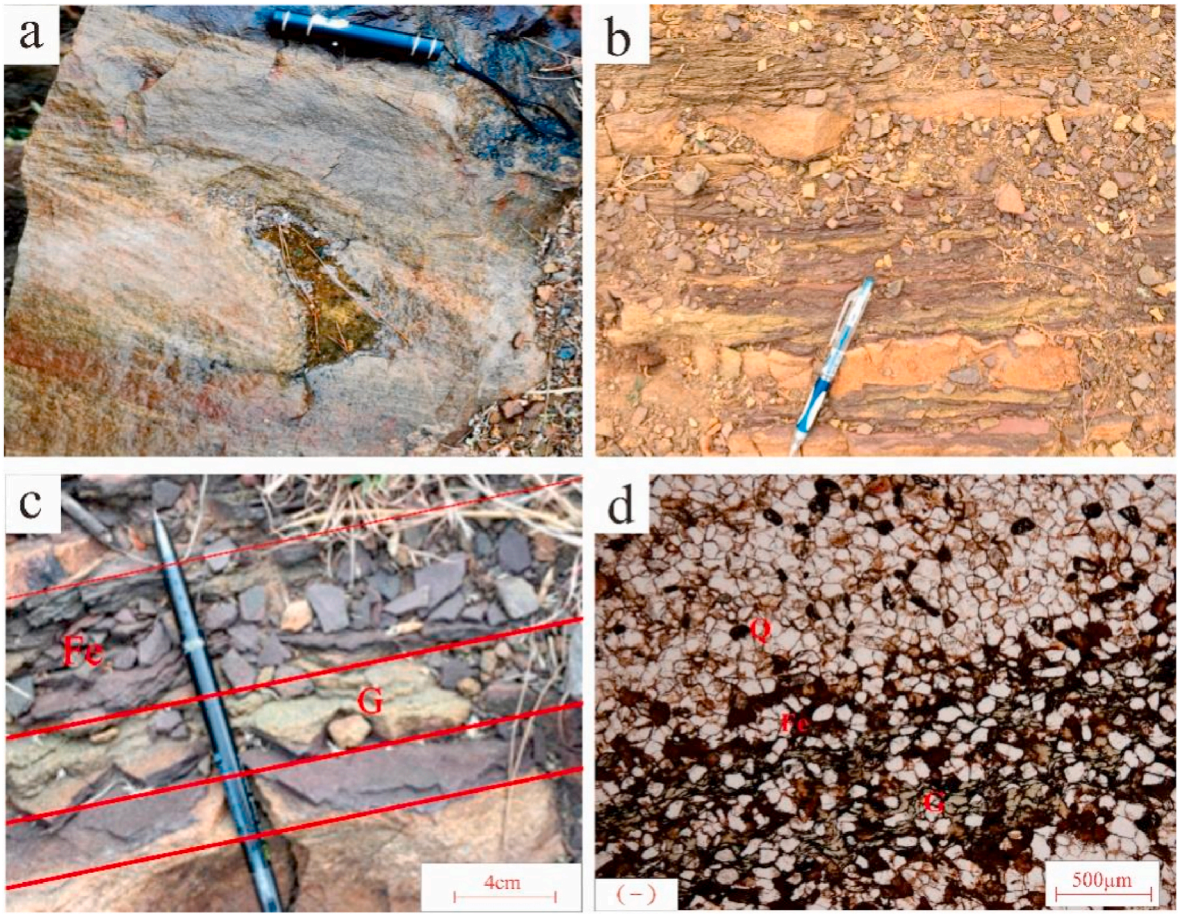

Fig. 15. Sedimentary characteristics of the Changlongshan Formation in the Longshan area. Notes: (a) Glauconite-bearing fine sandstone, with cross-bedding; (b) Glauconite-bearing siltstone, with horizontal bedding; (c) Interbeded glauconite sandstone and ferruginous sandstone; (d) Microscopic images of interbeded glauconite sandstone and ferruginous sandstone. Q-Quartz; G-Glauconite; Fe- Ferrum.

et al., 2020; Mei et al., 2008). Modern glauconites are formed in continental shelf margins, upper continental slopes and subtidal shallow shoal environments (Hegab et al., 2016; Wang and Lin, 1979). Previous studies (Chenet al., 2012; Chu et al., 2022; Guo et al., 2019; Wang et al., 2000; Zhang et al., 2017b) when combined with field profile observations and rock type studies, suggest that the Xiamaling Formation could be a clastic neritic-tidal flat deposits in the North China. Glauconites are mainly distributed in the subaqueous siltstones and fine sandstones of the subtidal zone in the lower part of the highstand systems tract (HST) (Fig. 2) (Zhang et al., 2022). The Changlongshan Formation is a set of clastic tidal flat deposits. Glauconites are distributed in the subtidal fine sandstones with cross-beddings (Fig. 15a) and associated with purplish red iron strips (Fig. 15c and d) in the lower part of the transgressive systems tract (TST) and the siltstones with horizontal beddings (Fig. 15b) in the top of the TST (Zhang et al., 2022) (Figs. 2 and 15). The collision between the North China Block and the adjacent terranes led to the uplift of the Xiamaling Formation (or Weixian Uplift) and the formation of collisional granites. The Neoproterozoic deposition was the result of the breakup of the Rodinia supercontinent. Quartz sandstones and glauconite sandstones of the Changlongshan Formation are the earliest sediments after the breakup of the Rodinia supercontinent, and they record the overlapping process in the early sea transgression process (Pan et al., 2013). The Neoproterozoic glauconite in the study area is widely developed in the subtidal sand flats and shoals of TST and HST, so it is difficult to distinguish the 'condensed segments' by the occurrence of glauconite (Amorosi, 2013; Chen, 1994; Ding, 1991). According to previous studies, glauconite formations are mostly distributed in the deep-water environment of the upper part of the mid-continental shelf with a low deposition rate (Banerjee et al., 2012, 2016; Deb and Fukuoka, 1998; Eder et al., 2007; Mei et al., 2008), and glauconite in the study area is distributed in the subtidal environment with a relatively high deposition rate. Therefore, it can be inferred that the low deposition rate in the deep-water environment is not the primary controlling factor for the formation of glauconite in the Neoproterozoic in North China, and the existence of glauconite cannot determine the specific systems tract of the sequence stratigraphy.

The formation of authigenic glauconite and iron-bearing minerals is regulated by the iron availability and redox conditions in seawater (Eder et al., 2007; Mandal et al., 2020; Tang et al., 2017; Baldermann et al., 2013; Baldermann et al., 2013; López-Quirós et al., 2019; Banerjee et al., 2012; Roy Choudhury et al., 2022a,b). The glauconite sandstones and ferruginous sandstones of the Changlongshan Formation are interbedded, and this kind of glauconite mostly exists in a cemented form (Fig. 15c and d). A sub-oxic depositional condition facilitates the formation of glauconite by mobilizing the irons in the Fe^{2+} state (Mandal et al., 2022; Roy Choudhury et al., 2022a,b; Su et al., 2016; Tang et al., 2017). Algal texture organisms have been found in the ferruginous sandstones of the Changlongshan Formation of North China, thus providing evidence for the existence of oxidation conditions (Mei et al., 2008; Zhang et al., 2020). Under the condition of insufficient or strong light, algal organisms will cause the difference of oxygen content in seawater, and thus lead to the rhythmic symbiosis between ferruginous sandstones and glauconite sandstones according to the different ratios of Fe^{2+} and Fe^{3+} (Mei et al., 2008; Zhang et al.,2020, 2022).

According to the differences in classification, distribution, morphology, color, and origin of different types of glauconites in this study (Table 3), the diagenesis and diagenetic stages of glauconite are comprehensively analyzed. Early studies suggested that glauconite was mainly formed by weathering of biotite from the sea floor during the syngenetic period (Bai and Dai, 1994; Burst, 1958; Chang, 1992; Chen, 1980; Chen and Duan, 1987; Hower, 1961). However, more and more studies have found that different kinds of glauconites have experienced different mechanical and chemical process or diagenesis in different burial stages. In this study, the formation of autochthonous granular glauconites of the Types I, II and III underwent early dissolution, metasomatism, maturation and later oxidation in the burial diagenetic stage. However, the Type IV autochthonous colloidal glauconites underwent cementation and oxidation in the early and late digenesis stags respectively. For the Type V allochthonous granular glauconites, they experienced autochthonous cementation or metasomatism of mica from the Xiamaling Formation in the early stage, followed by re-transport and allogenic redeposition in the later stage (Table 3). In addition, glauconite cements are found between the edges of quartz overgrowth and the quartz grains (Fig. 3j). It shows that the formation of glauconite should be later than the overgrowth of quartz, and may be formed in the later diagenetic stage. Therefore, glauconite can be formed in different diagenetic stages as long as suitable geological conditions are available.

5. Conclusions

(1) In the Longshan area, the Qingbaikou glauconites have granular, cementitious, clastic pseudomorphic, pigment-infested and halo - rimmed aggregated forms. Based on the variations in their color, morphology and chemical composition, these glauconites are classified into Type I - green granular glauconite with high K_2O and low TFeO content; Type II - yellow-green glauconite with low K_2O content; Type III - yellow-brown granular glauconite with strong oxidation; Type IV - yellow colloidal glauconite, whose chemical formula is difficult to derive; Type V - dark brown clastic glauconite, where its chemical composition has been altered to iron oxides.

(2) The formation of glauconite is controlled by source rocks and redox conditions. The glauconites in the Changlongshan Formation are sourced from iron components, glauconites and feldspar-rich rocks in the underlying Xiamaling Formation and the lower Changlongshan Formation.

(3) Types I granular glauconites exhibit high K_2O, Al_2O_3, SiO_2 and MgO, and low TFeO contents. The Type I granular glauconite follows a similar evolutional trend with the 'pseudomorphic replacement' theory. Types II granular glauconites show a general evolutional trend with layer lattice theory. Type III granular glauconites were formed by early pseudomorphic replacement or

Table 3
Classification and characteristics of the glauconites developed in the Qingbaikou System of the Longshan area, Beijing.

Classifications	Formation	Types	Genesis mechanism	Mechanical and chemical actions	Color and morphology
Autochthonous glauconite	Xiamaling and Changlongshan Formations	Type I	Pseudomorphic replacement	Dissolution and metasomatism	Light green granular or pigment-infested shape
		Type II	Layer lattice	Dissolution and metasomatism	Yellow-green granular
		Type III	Pseudomorphic replacement or layer lattice + alteration	Dissolution, metasomatism and oxidation	Yellow-brown granular
		Type IV	Autogenous precipitation + alteration	Cementation and oxidation	Yellow-brown colloidal or halo – rimmed
Allochthonous glauconite	Changlongshan Formation	Type V	Autogenous cementation or layer lattice + re-transportation + allochthonous re-deposition	Cementation or metasomatism followed by transport and deposition	Dark brown round or oval granular

layered lattice genesis combining later alteration. Type IV colloidal glauconites underwent early authigenic cementation and late oxidization. Type V detrital granular glauconites were formed by later re-transportation and allochthonous re-deposition of authigenic glauconite or mica pseudomorphic glauconite.

(4) The Neoproterozoic glauconite in the study area is widely developed in the subtidal sand flats and shoals of TST and HST, implying that the low deposition rate in the deep water environment is not the primary controlling factor for the formation of glauconite, and the existence of glauconite cannot determine the specific system tract of sequence stratigraphy. Different kinds of glauconites have experienced different mechanical and chemical processes or diagenesis in different stages.

Author contributions section

The first author (Qin Zhang) is responsible for the method and writing of the article.

The co-authors Chen Zhou, Shifa Zhu, Hanyun Tian and Zeping Song are responsible for the experiments and mapping.

The co-author Ronald J Steel provided important writing ideas and guidance.

Declaration of competing interest

The authors declare that they have no known competing financial interests or personal relationships that could have appeared to influence the work reported in this paper.

Data availability

Data will be made available on request.

Acknowledgements

This study was supported by the National Natural Science Foundation of China (Grant No. 41872134 and No. 41302081).

References

Absar, N., 2021. Mineralogy and geochemistry of siliciclastic miocene cuddalore formation, cauvery basin, south India: imlications for provenance and paleoclimate. Journal of Palaeography 10 (4), 602–630.
Adriaens, R., Vandenberghe, N., Elsen, J., 2014. Natural clay-sized glauconite in the neogene deposits of the campine basin (Belgium). Clay Clay Miner. 62 (1), 35–52.
Amorosi, A., 1994. The glaucony-bearing horizon of the lower miocene bisciarn formation (Umbria-Marche apennines). Giorn. Geol. 56 (1), 7–16.
Amorosi, A., 1997. Detecting compositional, spatial, and temporal attributes of glaucony: a tool for provenance research. Sediment. Geol. 109 (1–2), 135–153.
Amorosi, A., Sammartino, I., Tateo, F., 2007. Evolution patterns of glaucony maturity: a mineralogical and geochemical approach. Deep Sea Res. Part II Top. Stud. Oceanogr. 54, 1364–1374.
Amorosi, A., Guidi, R., Mas, R., Falanga, E., 2012. Glaucony from the Cretaceous of the Sierra de Guadarrama (Central Spain) and its application in a sequence-stratigraphic context. Int. J. Earth Sci. 101 (2), 415–427.
Bai, J., Dai, F.Y., 1994. The early Precambrian crust evolution of China. Bull. Chin. Acad. Geol. Sci. Z2, 73–87 (in Chinese with English abstract).
Baioumy, H.M., Boulis, S.N., 2012a. Glauconites from the bahariya oasis: an evidence for cenomanian marine transgression in Egypt. J. Afr. Earth Sci. 70 (1), 1–7.
Baioumy, H., Boulis, S., 2012b. Non-pelletal glauconite from the campanian qusseir formation, Egypt: implication for glauconitization. Sediment. Geol. 249 (1), 1–9.
Baldermann, A., Warr, L.N., Grathoff, G.H., Dietzel, M., 2013. The rate and mechanism of deep-sea glauconite formation at the Ivory Coat-Ghana marginal ridge. Clay Clay Miner. 61 (3), 258–276.
Banerjee, S., Jeevankumar, S., Eriksson, P.G., 2008. Mg-rich ferric illite in marine transgressive and highstand systems tracts:Examples from the Paleoproterozoic Semri Group, central India. Precambrian Res. 162 (1–2), 212–226.
Banerjee, S., Chattoraj, S.L., Saraswati, P.K., Dasgupta, S., Bumby, A., 2012. The origin and maturation of lagoon alglauconites: a case study from the Oligocene Maniyara Fort Formation, western Kutch, India. Geol. J. 47 (4), 357–371.
Banerjee, S., Mondal, S., Chakraborty, P.P., Meena, S.S., 2015. Distinctive compositional characteristics and evolutionary trend of precambrian glaucony: example from bhalukona formation, Chhattisgarh basin, India. Precambrian Res. 270, 33–48.
Banerjee, S., Bansal, U., Pande, K., Meena, S.S., 2016a. Compositional variability of glauconites within the upper cretaceous karai shale formation, cauvery basin, India: implications for evaluation of stratigraphic condensation. Sediment. Geol. 331, 12–29.
Banerjee, S., Bansal, U., Thorat, A.V., 2016b. A review on paleogeographic implications and temporal variation in glaucony composition. J. Palaeogeogr. 5 (1), 435–484.
Bansal, U., Banerjee, S., Ruidas, D.K., Pande, K., 2018. Origin and geochemical characterization of the glauconites in the upper cretaceous lameta formation, narmada basin, central India. J. Palaeogeogr. 7 (2), 3–20.
Burst, J.F., 1958. Mineral heterogeneity in"glauconite"pellets. Am. Mineral. 43, 481–497.
Cecil, M.R., Ducea, M.N., 2011. K-Ca ages of authigenic sediments: examples from Paleozoic glauconite and applications to low-temperature thermochronometry. Int. J. Earth Sci. 100 (8), 1783–1790.
Chafetz, H.S., 2007. Paragenesis of the Morgan Creek Limestone,late Cambrian,central Texas:constraints on the formation of glauconite. Deep Sea Res. Part II Top. Stud. Oceanogr. 54, 1350–1363.
Chang, Q.M., 1992. Research on the concentration features and the sedimental context of glauconite in Shimenzhai Area,Qinhuangdao. Journal of Tangshan Institute of Technology (2), 54–58 (in Chinese with English abstract).
Chen, R.J., 1980. The characteristics of glaucony in some areas of our country and its significance to the analysis of relative environment. Geological sciences 15 (1), 65–75 (in Chinese with English abstract).
Chen, R.K., 1994. Key stratigraphic units-glauconitic condensed sections in the Cambrian depositional sequences on the north China platform. Sediment. Facies Palaeogeogr. 14 (6), 25–34 (in Chinese with English abstract).
Chen, L.R., Duan, W.M., 1987. Formation of glauconite as infillings of organism. Acta Sedimentol. Sin. 5 (3), 171–179 (in Chinese with English abstract).
Chen, S.H., Li, Y., Hu, Z.W., Li, X.P., Ma, Y.K., Zhu, P., Chen, A.Q., 2014. The cause of formation, indicating sedimentary facies and age significance of glaucony. Journal of rock and mineralogy 33 (5), 971–979 (in Chinese with English abstract).
Chu, Q.Z., You, Z.Y., Lin, J.Y., Zhang, H.Y., Han, S.W., Gao, W.L., Hamza, I.M.K., 2022. Mineral characteristics and formation environment of glauconite in upper archean of Liujiang Basin, qinhuangdao, hebei province: a case study of Changlongshan Formation in jiguanshan. Acta Geosci. Sin. 43 (1), 25–37 (in Chinese with English abstract).
Condie, K.C., Wilks, M., Rosen, D.M., Zlobin, V.L., 1991. Geochemistry of metasediments from the precambrian hapschan series, eastern anabar shield, siberia. Precambrian Res. 50 (1–2), 37–47.
Dasgupta, S., Chaudhuri, A.K., Fukuoka, M., 1990. Compositional characteristics of glauconitic alterations of K-feldspar from India and their implications. J. Sediment. Petrol. 60, 277–281.
Deb, S.P., Fukuoka, M., 1998. Fe-illites in a Proterozoic deep marine slope deposit of the Pranhita Godavari valley: their origin and environmental significance. J. Geol. 106, 741–749.
Diaz, E., Prasad, M., Mavko, G., Dworkin, J., 2003. Effect of glauconite on the elastic properties, porosity and permeability of reservoir rocks. Lead. Edge 22 (1), 42–45.
Ding, S.L., 1991. The property of glauconite and its facies-indicating significance in longtan formation nayong District guizhou province. Coal Geol. Explor. 19 (4), 10–15 (in Chinese with English abstract).
Eder, V.G., Martín-Algarra, A., Sánchez-Navas, A., Zanin, Y.N., Zamirailova, A.G., Lebedev, Y.N., 2007. Depositional controls on glaucony texture and composition, upper jurassic, west siberian basin. Sedimentology 54 (6), 1365–1387.
Fan, W.B., 2015. Geological characteristics and research progress of the mesoproterozoic Xiamaling Formation in the NorthNorth China craton: a review of the Xiamaling Formation in the past century. Geol. Rev. 61 (6), 1383–1406 (in Chinese with English abstract).
Fernández-Landero, S., Fernández-Caliani, J.C., 2021. Mineralogical and crystal-chemical constraints on the glauconite-forming process in Neogene sediments of the Lower Guadalquivir Basin (SW Spain). Minerals 11 (6), 578.
Fischer, H., 1990. Glauconite formation: discussion of the terms authigenic, perigenic, allogenic and meta-allogenic. Eclogae Geol. Helv. 83 (1), 1–6.
Fürsich, F.T., Alberti, M., Pandey, D.K., Chaskar, K., Bhosale, S., 2021. Facies analysis and palaeoecology of the jurassic spiti shale Formation in the spiti area, northern India. J. Palaeogeogr. 10 (4), 438–462, 2021.
Gopalan, K., 2008. Conjunctive K-Ca and Rb-Sr dating of glauconies. Chem. Geol. 247, 119–123.
Gu, X.X., Liu, J.M., Zheng, M.H., Tang, J.X., Qi, L., 2002. Provenance and tectonic setting of the proterozoic turbidites in Hunan,South China: geochemical evidence. J. Sediment. Res. 72 (3), 393–407.
Guo, Q.H., Jin, Z.K., Zhu, X.E., Li, S., Shi, Y.T., Wang, J.J., Chen, Y.F., 2019. Sedimentary facies evolution of the neoproterozoic in Qingbaikou area of jingxi depression, yanshan region. J. Palaeogeogr. 21 (3), 422–430 (in Chinese with English abstract).
Harder, H., 1980. Syntheses of glauconite at surface temperatures. Clay Clay Miner. 28 (3), 217–222.
Harris, L.C., Whiting, B.M., 2000. Sequence-stratigraphic significance of Miocene to Pliocene glauconite-rich layers, on-and offshore of the US Mid-Atlantic margin. Sediment. Geol. 134 (1), 129–147.
Hegab, O.A., Serry, M.A., Anana, T.I., El-Wahed, A.G.A., 2016. Facies analysis, glauconite distribution and sequence stratigraphy of the middle Eocene Qarara Formation, El-Minya area, Egypt. *Egyptian Journal of Basic and Applied* Sciences 3 (1), 71–84.

Hou, E., Cong, T., Xie, X., 2020. Ground surface fracture development characteristics of shallow double coal seam staggered mining based on particle flow. Journal of Mining and Strata Control Engineering 2 (1), 013521. https://doi.org/10.13532/j.jmsce.cn10-1638/td.2020.01.002.
Hower, J., 1961. Some factors concerning the nature and origin of glauconite. Am. Mineral. 46 (3), 313–334.
Huang, B., Gao, Y.J., Mu, Z.G., 1998. Introduction to the singlegrain ^{40}Ar-^{39} Ar dating of glauconies. Adv. Earth Sci. 13 (4), 90–91.
Jafarzadeh, M., Choudhury, T.R., Taheri, A., Banerjee, S., Jafarian, A., 2020. Glauconite within albian-cenomanian aitamir formation, kopet-dagh basin, northeastern Iran: origin and implications of cretaceous seawater. Arabian J. Geosci. 13, 1236.
Kazerouni, A.M., Poulsen, M.L.K., Friis, H., Svendsen, J.B., Hansen, J.P.V., 2013. Illite/smectite transformation in detrital glaucony during burial diagenesis of sandstone: a study from Siri Canyon-Danish North Sea. Sedimentology 60 (3), 679–692.
Li, X., 2014. Formation mechanism and controlling factors of cretaceous glauconite in zanda, southwest tibet. Journal of rock and mineralogy 33 (5), 906–916.
Li, L., Zhang, X., Deng, H., 2020. Mechanical properties and energy evolution of sandstone subjected to uniaxial compression with different loading rates. Journal of Mining and Strata Control Engineering 2 (4), 043037. https://doi.org/10.13532/j.jmsce.cn10-1638/td.20200407.001.
López-Quirós, A., Escutia, C., Sánchez-Navas, A., Nieto, F., Garcia-Casco, A., Martín-Algarra, A., Evangelions, D., Salabarnada, A., 2019. Glaucony anthogenesis, maturity and alteration in the Weddell Sea: an indicator of paleoenvironmental conditions before the onset of Antarctic glaciation. Sci. Rep. 9, 13580.
Mandal, S., Banerjee, S., Sarkar, S., Mondal, I., Roy Choudhury, T., 2020. Origin and sequence stratigraphic implications of high-alumina glauconite within the Lower Quartzite, Vindhyan Supergroup. Mar. Petrol. Geol. 112, 104040.
Mandal, S., Roy Choudhury, T., Das, A., Sarkar, S., Banerjee, S., 2022. Shallow marine glauconitization during the Proterozoic in response to intrabasinal tectonics: a study from the Proterozoic Lower Bhander Sandstone, Central India. Precambrian Res. 372, 106596.
McLennan, S.M., 1993. Weathering and global denudation. J. Geol. 101 (2), 295–303.
Mei, C.J., 2018. Glauconitization and pyritization of stromatolites: a case of the mesoproterozoic Tieling Formation at jixian section, Tianjin, North China. J. Palaeogeogr. 20 (3), 453–464 (in Chinese with English abstract).
Mei, M.X., Yang, J., Gao, J.H., Meng, Q.F., 2008. Glauconites formed in the high-energy shallow marine environment of the late Mesoproterozoic: a case study from Tieling Formation at Jixian section in Tianjin, North China. Earth Sci. Front. 15 (4), 146–158 (in Chinese with English abstract).
Odin, G.S., Fullagar, P.D., 1988. Geological significance of the glaucony facies. Green Marine Clays 45, 295–332.
Odin, G.S., Matter, A., 1981. De glauconiarum origine. Sedimentology 28 (5), 611–641.
Pan, J.G., Qu, Y.Q., Ma, R., Pan, Z.K., Wang, H.L., 2013. Sedimentary and tectonic evolution of the meso-neoproterozoic strata in the northern margin of the NorthNorth China Block. Geol. J. China Univ. 19 (1), 109–122 (in Chinese with English abstract).
Qu, Y.Q., Pan, J.G., Liang, L.D., Yang, Z.F., Wang, H.L., 2012. The properties of unconformities in the Proterozoic in the Yanliao rift trough. Sediment. Geol. Tethyan Geol. 32 (2), 11–22 (in Chinese with English abstract).
Roy Choudhury, T., Banerjee, S., Khanolkar, S., Saraswati, P.K., Meena, S.S., 2021. Glauconite authigenesis during the onset of the paleocene-eocene thermal maximum: a case study from the khuiala Formation in jaisalmer basin, India. Palaeogeogr. Palaeoclimatol. Palaeoecol. 571, 110388.
Roy Choudhury, T., Banerjee, S., Khanolkar, S., Meena, S.S., 2022a. Paleoenvironmental conditions during the paleocene–eocene transition imprinted within the glauconitic giral member of the barmer basin, India. Minerals 12 (1), 56.
Roy Choudhury, T., Sunder Raju, P.V., Shaikh, T., Banerjee, S., 2022b. An assessment of alternate fertilizer potential of glauconite deposits in India using simple beneficiation methods. J. Geol. Soc. India 98, 181–184.
Rudmin, M., Banerjee, S., Mazurov, A., 2017. Compositional variation of glauconites in upper cretaceous-paleogene sedimentary iron-ore deposits in south-eastern western siberia. Sediment. Geol. 355, 20–30.
Sánchez-Navas, A., Martín-Algarra, A., Eder, V.G., Reddy, B.J., Nieto, F., Zanin, Y.N., 2008. Color, mineralogy and composition of upper jurassic west siberian glauconite: useful indicators of paleoenvironment. Can. Mineral. 46 (5), 1249–1268.
Smith, P.E., Evensen, N.M., York, D., 1998. Single-grain Ar-40-Ar-39 ages of glauconies: implications for the geologic time scale and global sea level variations. Sicence 279 (5356), 1517–1519.
Stille, P., Clauer, N., 1994. The process of glauconitization:chemical and isotopic evidence. Contrib. Mineral. Petrol. 117 (3), 253–262.
Strickler, M.E., Ferrell, R.E., 1990. Fe substitution for Al in glauconite with increasing diagenesis in the first Wilcox sandstone (Lower Eocene), Livingston Parish, Louisiana. Clay Clay Miner. 38 (1), 69–76.
Su, S.Q., Chuan, X.Y., Ma, H.W., zhang, P., 2016. Mineralogical characteristics of glauconite and its applicantion research. Ind. Miner. Process. 45 (2), 30–35 (in Chinese with English abstract).
Tang, D.J., Shi, X.Y., Ma, J.B., Shi, Q., 2016. Mesoproterozoic glaucony as a potential mineral proxy for shallow chemocline in the Precambrian ocean. Earth Sci. Front. 23 (6), 219–235 (in Chinese with English abstract).
Tang, D.J., Shi, X.Y., Ma, J.B., Jiang, G.Q., Zhou, X.Q., Shi, Q., 2017. Formation of shallow-water glaucony in weakly oxygenated Precambrian ocean: an example from the Mesoproterozoic Tieling Formation in North China. Precambrian Res. 294, 214–229.
Tounekti, A., Boukhalfa, K., Roy Choudhury, T., Soussi, M., Banerjee, S., 2021. Global and local factors behind the authigenesis of Fe-silicates (Glauconite/Chamosite) in Miocene strata of Northern Tunisia. J. Afr. Earth Sci. 184, 104342.
Tutolo, B.M., Kiesel, T., Luhmann, A.J., Solheid, P., Seyfried, W.E., 2020. Experimental evaluation of the role of redox during glauconite-CO2-brineinteractions. Appl. Geochem. 115, 104558.
Wang, Y.W., Lin, Z.H., 1979. Glauconite in modern marine sediments. Mar. Sci. Bull. 4, 33–50 (in Chinese with English abstract).
Wang, J., Wang, X.L., 2021. Seepage characteristic and fracture development of protected seam caused by mining protecting strata. Journal of Mining and Strata Control Engineering 3 (3), 033511. https://doi.org/10.13532/j.jmsce.cn10-1638/td.20201215.001.
Wang, L.F., Li, W.X., Luo, J.L., Hu, W.B., 2000. The study on sedimentary facies of changlongshan Formation of neoproterozoic era in huailai, hebei. World Geology (2), 138–143 (in Chinese with English abstract).
Wang, T., Zhu, X.M., Dong, Y.L., Chen, H.H., Su, B., Liu, Y., Wu, Y., 2020. Reconstruction of paleo-sedimentary background based on trace element analysis: taking the Anji Haihe Formation of the Paleogene in the northwestern margin of Junggar Basin as an example. Acta Geol. Sin. 94 (12), 3830–3851 (in Chinese with English abstract).
Wu, J.J., 1992. The property and sedimentary environment of glauconite of Longtan Formation in south Jiangsu Province. J. Stratigr. 16 (3), 210–215 (in Chinese with English abstract).
Wu, F.D., Lu, Y.C., Chen, P., Zhou, P., 1997. The discovery and significance of glauconites in the huagong Formation of the oligocene, xihu Depression,East China sea. Acta Sedimentol. Sin. 15 (3), 158–161 (in Chinese with English abstract).
Xu, Y.H., Zhao, T.P., Chen, W., 2010. The discovery and geological significance of glauconites from the paleoproterozoic xiong'er group in the southern part of the NorthNorth China craton. Acta Sedimentol. Sin. 28 (4), 671–675 (in Chinese with English abstract).
Yang, X.F., Xie, Y.F., Zhang, Z.W., Ma, Z.Z., Guo, C.E., Zhou, Y.B., Wang, D.D., Liu, Y.M., Zhao, Y.B., 2016. Genetic type and sedimentary geological significance of Cretaceous glauconite in Oriente Basin, Ecuador. Earth Sci. 41 (10), 1696–1708 (in Chinese with English abstract).
Yang, T.Y., Shen, Y.L., Zhang, T., Li, Z.F., Tong, G.C., Liu, J.B., 2020. Investigation of the genesis of glauconite in the cambrian xuzhuang Formation in Dabeiwang,Xuzhou. Geol. J. China Univ. 26 (3), 276–285 (in Chinese with English abstract).
Zhang, T., 2018. Discussion on the Origin and Geological Significance of Cambrian Sea Greenstone in Dabeiwang Section of Xuzhou. China Mining University (in Chinese with English abstract).
Zhang, Q., Tutolo, B.M., 2021. Geochemical evaluation of glauconite carbonation during sedimentary diagenesis. Geochem. Cosmochim. Acta 306, 226–244.
Zhang, Q., Mei, X.H., Xie, Y.F., Wang, Q.X., Li, C.X., Yang, X.F., Du, H.Y., Lu, J.J., 2016. Characteristics of different types of glauconite and their classification systems. Oil Gas Geol. 37 (6), 952–963 (in Chinese with English abstract).
Zhang, C., Li, J.A., Jiao, J.W., Ding, Y., Shao, L.Y., 2017a. A study of sedimentary facies and sequence stratigraphy of the Changlongshan Formation (Qingbaikou) in xiaweidian area, west mountain of beijing. J. Palaeogeogr. 19 (6), 955–964 (in Chinese with English abstract).
Zhang, X.K., Cai, Y.F., Bai, L.J., Pan, Y.G., 2017b. The experimental study of mineral transforming from montmorillonite to glauconite. Geol. Rev. 63 (2), 471–483 (in Chinese with English abstract).
Zhang, Q., Wang, B.H., Zhou, C., Sun, Z.Y., Mei, X.H., Yuan, C.S., Wang, k., 2020. Characteristics and genesis of iron Formation in the changlongshan Formation of Qingbaikou system in the ming tombs area, beijing. J. Palaeogeogr. 22 (3), 570–586 (in Chinese with English abstract).
Zhang, Q., Zhou, C., Tian, H.Y., Zhu, X.M., Wu, X.S., Song, Z.P., Wang, K., 2022. Sequence stratigraphic framework and model of mixed siliciclastic-carbonate rocks in the Qingbaikouan System, Longshan area, North China. Oil Gas Geol. 43 (4), 792–803 (in Chinese with English abstract).
Zhou, H.R., Mei, M.X., Luo, Z.Q., Xing, K., 2006. Sedimentary sequence and stratigraphic framework of the neoproterozoic Qingbaikou system in the yanshan region,North China. Earth Sci. Front. 13 (6), 280–290 (in Chinese with English abstract).
Zhou, X.Q., Li, N., Liang, G.S., Li, L., Tang, D.J., 2009. Sedimentary significance of the autochthonous glauconite in stromatoliticlime stones of the mesoproterozoic Tieling Formation in jixian, Tianjin, North China. Geol. Bull. China 28 (7), 985–990 (in Chinese with English abstract).
Zhu, S.X., Liu, H., Hu, J., 2012. On the disintegration of the neoproterozoic qingbaikouan system in yanshan range, North China. Geological Survey And Research 35 (2), 81–95 (in Chinese with English abstract).